JGR Solid Earth

RESEARCH ARTICLE
10.1029/2025JB033454

Key Points:

- We develop a simple reference model that highlights the effect of fault roughness on the migration of injection-induced seismicity
- Seismicity front often migrates more slowly than pressure front and depends strongly on fault roughness and initial stress environment
- Back-fronts occur because earthquake stress drops push the fault farther from criticality near the injector

Supporting Information:

Supporting Information may be found in the online version of this article.

Correspondence to:
H.-F. Lin,
hsiao-fan.lin@geoazur.unice.fr

Citation:
Lin, H.-F., Candela, T., & Ampuero, J.-P. (2026). Fault roughness controls seismicity front migration during fluid injection. *Journal of Geophysical Research: Solid Earth*, *131*, e2025JB033454. https://doi.org/10.1029/2025JB033454

Received 25 NOV 2025
Accepted 11 FEB 2026

Author Contributions:
Conceptualization: Hsiao-Fan Lin, Thibault Candela, Jean-Paul Ampuero
Formal analysis: Hsiao-Fan Lin, Thibault Candela, Jean-Paul Ampuero
Funding acquisition: Thibault Candela, Jean-Paul Ampuero
Methodology: Hsiao-Fan Lin, Thibault Candela, Jean-Paul Ampuero
Project administration: Thibault Candela, Jean-Paul Ampuero
Software: Hsiao-Fan Lin, Thibault Candela
Supervision: Thibault Candela, Jean-Paul Ampuero
Visualization: Hsiao-Fan Lin
Writing – original draft: Hsiao-Fan Lin

Fault Roughness Controls Seismicity Front Migration During Fluid Injection

Hsiao-Fan Lin[1,2], **Thibault Candela**[2], **and Jean-Paul Ampuero**[1]

[1]Université Côte d'Azur, IRD, CNRS, Observatoire de la Côte d'Azur, Géoazur, Sophia Antipolis, Valbonne, France,
[2]TNO, Geological Survey of the Netherlands, Utrecht, The Netherlands

Abstract The increasing occurrence of injection-induced earthquakes has raised public concern and highlighted the importance of understanding subsurface processes and mechanisms to assess induced seismic hazards and risks. We develop a simple physics-based model to investigate how fault roughness controls the migration of seismicity during fluid injection. Simulations reproduce key observations: diffusion-like seismicity migration and back-fronts. The apparent diffusivity of seismicity fronts can deviate significantly from the hydraulic diffusivity. Faults, with realistic roughness, generally display slow seismicity migration, producing apparent diffusivities far below the hydraulic values. Thus, seismicity fronts often lag behind the pressure front, especially at low initial stresses and small roughness amplitudes. Only in the rare case of very rough faults stressed very close to failure, apparent diffusivity can exceed the hydraulic diffusivity, leading to seismicity fronts that outpace pressure fronts. In our model, the emergence of a back-front near the injector well during continuous injection is caused by stress released by early rupture events. These findings demonstrate that fault roughness and initial stress environment control the migration speed of induced seismicity through their influence on the criticality of the fault and stress transfer, and provide valuable insights to interpret seismicity migration patterns in fluid injection scenarios.

Plain Language Summary Earthquakes can be triggered during fluid injection into the subsurface, such as during geothermal energy production and wastewater disposal. These induced earthquakes usually migrate outward from the injection well, and the migration speed is often used to estimate how quickly fluid pressure diffuses through the rock. Our results show that this relationship can be misleading. Using a simple model, we examine how the typical roughness of faults influences seismicity migration. We find that earthquake migration is typically slower than the pressure diffusion, more so when the fault is smoother or the initial stress is lower. Our model also produces zones where earthquakes are inhibited after large events near the injector. These findings demonstrate that fault roughness and stress transfer are key controls on seismicity migration and should be considered when interpreting migration patterns in terms of fluid diffusion.

1. Introduction

Induced seismicity has been observed in various human activities involving fluid injection in the subsurface, such as wastewater disposal (Ellsworth, 2013), geothermal reservoir stimulation (Deichmann & Giardini, 2009) and hydraulic fracturing (Eyre et al., 2020). One of the most striking features of injection-induced seismicity is that it migrates: the volume covered by the earthquake hypocenters expands with time. Seismicity migration is often quantified by estimating diffusivity from the spatio-temporal pattern of seismicity under the assumption that the seismicity front coincides with a pore pressure front (Shapiro et al., 1997). The diffusivity inferred from seismicity, called hereafter "apparent diffusivity", is often assimilated to the hydraulic diffusivity, which spans a wide range of values from $\sim 10^{-9}$ to $\sim 10^{3}$ m^2/s according to in situ field experiments (Doan et al., 2006; Guglielmi et al., 2015). However, it has been recognized that, in theory, the initial stress environment could influence the apparent diffusivity (Bhattacharya & Viesca, 2019; Sáez et al., 2022; Talwani & Acree, 1984): depending on how far from criticality a fault is before injection, the seismicity front can outpace or lag behind the pressure front, meaning the apparent diffusivity can be higher or lower than the hydraulic diffusivity.

An important factor that controls the state of stress of a fault is its geometry, and in particular its roughness. Modeling studies of induced seismicity often assume a planar fault or a uniform pre-stress (De Barros et al., 2021; Garagash & Germanovich, 2012; Segall & Lu, 2015; Wynants-Morel et al., 2020). Previous studies have shown that heterogeneous fault strength plays a key role in controlling the spatio-temporal evolution of injection-induced

Writing – review & editing: Hsiao-Fan Lin, Thibault Candela, Jean-Paul Ampuero

seismicity. Rothert and Shapiro (2007) demonstrate how heterogeneous critical pressure affects the migration of fluid-induced microseismicity. However in many of these studies, the spatial distribution of fault strength and/or distance to criticality were stochastic without any physical constraints. For instance, Rothert and Shapiro (2007) and Hummel and Shapiro (2012) incorporated randomly heterogeneous pre-stress distributions, these distributions are rarely constrained by direct observations. Natural faults, in contrast, exhibit measurable and well-characterized fault roughness over a wide range of scales (Brodsky et al., 2016; Candela et al., 2009, 2012; Power et al., 1987). Several studies show that fault roughness can influence nucleation, propagation and arrest of ruptures (Fang & Dunham, 2013; Ozawa et al., 2019; Tal et al., 2018). Laboratory experiments also demonstrate how fault roughness affects the spatial distribution of hypocenters and slows down injection-induced fault slip (Wang et al., 2024). However, the effect of fault roughness on the migration of injection-induced seismicity has never been addressed.

The primary objective of this study is to examine how fault roughness and initial stress environment influence the migration of injection-induced seismicity. By incorporating roughness into our fault model, we introduce a physically based source of heterogeneity that influences both the along-fault initial stress state and the stress redistribution during rupture events. A key question addressed in prior literature is whether seismicity can migrate faster than fluid diffusion (Cappa et al., 2022; Wynants-Morel et al., 2020). Bhattacharya and Viesca (2019) and Sáez et al. (2022) analyzed the evolution of an injection-induced circular aseismic rupture to explore whether the rupture front can propagate faster than the fluid pressure front. Our study builds on these single-rupture models by analyzing the nucleation front of multiple rupture events during continuous fluid injection. Using models that account for fault roughness and varying levels of criticality, our analysis reveals whether and under what conditions the seismicity front can outpace the pressure front.

2. Methods

We employ a physics-based model to simulate multiple rupture events induced by fluid injection on a rough fault (Candela et al., 2019). The model assumes that fluid is injected at a constant rate at the center of the fault and diffuses only along the fault. Our model accounts only for the direct pressure effect on the effective normal stress and does not consider thermoelastic or poroelastic stress changes. Fault slip is governed by the Mohr-Coulomb failure criterion with instantaneous frictional weakening. Stress is redistributed statically during each rupture. Heterogeneity is introduced only by the effects of fault roughness on the initial stresses and on stress transfer during rupture events. All model parameters listed in Table 1, including the friction coefficients and fluid transport properties, are kept spatially uniform with no time dependency and are set to reasonable values based on the literature. This intentionally simple model allows us to capture the interplay between fluid injection, fault roughness, and rupture propagation. The modeling assumptions and procedures are described in detail in the remainder of this section.

2.1. Pore Pressure Distribution

We conceptualize the fault as a rough surface at a macroscopic scale (Figure 1b), while at a microscopic scale, it is composed of two rough, unmatched surfaces in partial contact, and separated by an average aperture h (Figure 1a). Even though the local aperture is spatially heterogeneous due to surface roughness, which might affect the flow rate according to the cubic law (Witherspoon et al., 1979):

$$\frac{Q}{\Delta H} \propto h^3 \tag{1}$$

where Q is the flow rate, ΔH is the difference in hydraulic head. Brown (1987) demonstrated that the cubic law can still apply to rough fractures when the aperture is defined as the average aperture. We thus consider the rough fracture characterized by homogeneous and isotropic average aperture h, permeability k, fluid viscosity η, and product of porosity and compressibility $\phi\beta$. Another conceptual model leading to the same governing equations is illustrated in Figure 1c, in which the rough fault surface is embedded in a gouge zone with uniform hydraulic properties and a constant thickness h.

The fault is traversed by a well, through which fluids are injected onto the fault, inducing pore pressure diffusion. Because the roughness, that is, height fluctuation, is small relative to the fault dimensions (as quantified in

Table 1
Model Parameters

Parameter	Value
Hurst exponent ζ	0.8
Roughness amplitude C	0.2% (low), 0.5% (medium), 0.8% (high)
Initial stress environment $K_0 = \sigma_h/\sigma_v$	0.65 (low stress), 0.63 (medium stress), 0.60 (high stress)
Static friction coefficient μ_s	0.6
Dynamic friction coefficient μ_d	0.55
Fracture permeability k	10^{-11} m^2
Average aperature h	0.1 m
Product of porosity and compressibility $\phi\beta$	2×10^{-8}, 10^{-8}, 5×10^{-9} 1/Pa
Fluid viscosity η	0.001 Pa·s
Hydraulic diffusivity $D_0 = \frac{k}{\phi\eta\beta}$	0.5, 1, 2 m^2/s
Mass injection rate $\dot{m}_{r_b}$	10 kg/s
Radius of well r_b	0.2 m
Fault length a	1,500 m
Fault width b	500 m
Slip type	Dip slip
Dip	70°
Strike	0°
Depth	2,500 m
Horizontal stress ratio $K_h = \sigma_h/\sigma_H$	0.9
Azimuth of σ_h	90°
Rock density ρ_r	2,500 kg/m^3
Fluid density ρ_w	1,000 kg/m^3
Gravitational acceleration g	9.8 m/s^2
Shear modulus μ	33 GPa
Poisson's ratio	0.25

Section 2.2), the difference between pressure diffusion on planar and weakly non-planar faults is negligible (Faraudo, 2002). We therefore adopt the diffusion solution on a planar fault as an adequate approximation. This reference planar fault (Figure 1b) is the average plane that passes through the modeled rough fault. Therefore, the spatio-temporal evolution of the pore pressure, as defined on the reference plane and mapped onto the rough fault surface, is governed by the diffusion equation:

$$\frac{\partial p}{\partial t} = D_0 \nabla^2 p \tag{2}$$

where p is the pore pressure, ∇^2 is the 2D Laplacian along the reference plane, and D_0 is the hydraulic diffusivity, which is equal to $\frac{k}{\phi\eta\beta}$.

We impose a constant fluid mass flux at the borehole wall with a mass injection rate $\dot{m}_{r_b}$, starting at $t = 0$:

$$\rho_w |\mathbf{q}(r = r_b, t \geq 0)| = \frac{\dot{m}_{r_b}}{2\pi r_b h} \tag{3}$$

where $\mathbf{q}$ represents the imposed flux vector, r represents the distance to the injector, r_b is the injection borehole radius, ρ_w is the fluid density, assumed equal to the density of groundwater; therefore, no buoyancy effect is involved. The imposed flux is related to pressure by Darcy's law (Dake, 1978):

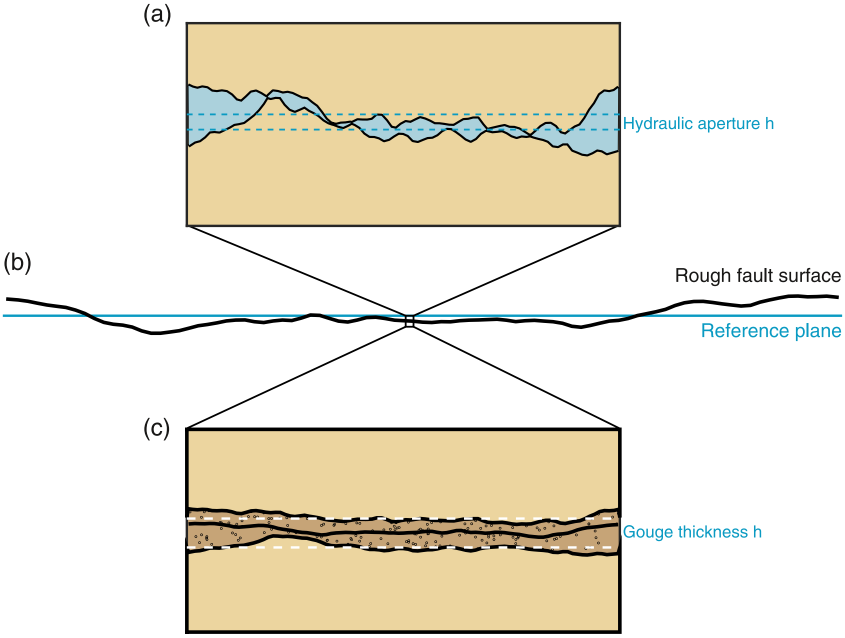

Figure 1. Schematic diagram of our conceptual model at (a) microscopic and (b) macroscopic scales. (c) Another conceptual model leading to the same governing equations.

$$\mathbf{q} = -\frac{k}{\eta}\nabla(p - \rho_w g z) \tag{4}$$

where g is the gravitational acceleration, and z denotes depth. We can decompose the total pressure p as

$$p = p_0 + \Delta p = \rho_w g z + \Delta p \tag{5}$$

where p_0 is the initial depth-dependent hydrostatic pore pressure, and Δp the pressure change induced by fluid injection. Combining Equations 4 and 5, we can see that the boundary condition on Δp does not depend on gravity, thus the diffusion of pressure changes in our model is driven solely by fluid injection.

At infinite distance from the injection borehole, the pore pressure equals the initial (pre-injection) pore pressure p_0:

$$\Delta p(r \rightarrow \infty, t) = 0 \tag{6}$$

The resulting pore pressure distribution along the fault as a function of distance from the injector (r) and time is (Bear, 1979; Martínez-Garzón et al., 2014; Mossop, 2001; Sáez et al., 2022; Theis, 1935):

$$\Delta p(r,t) = P_v E_1\left(\frac{r^2}{4D_0 t}\right)H(t) \tag{7}$$

$$P_v = \frac{\dot{m}_{r_b}\eta}{4\pi\rho_w k h} \tag{8}$$

where P_v is a characteristic pressure, E_1 is the exponential integral of the first kind (Abramowitz & Stegun, 1948), and H is the Heaviside function Representative examples of pressure histories are shown in Figure S1 of Supporting Information S1.

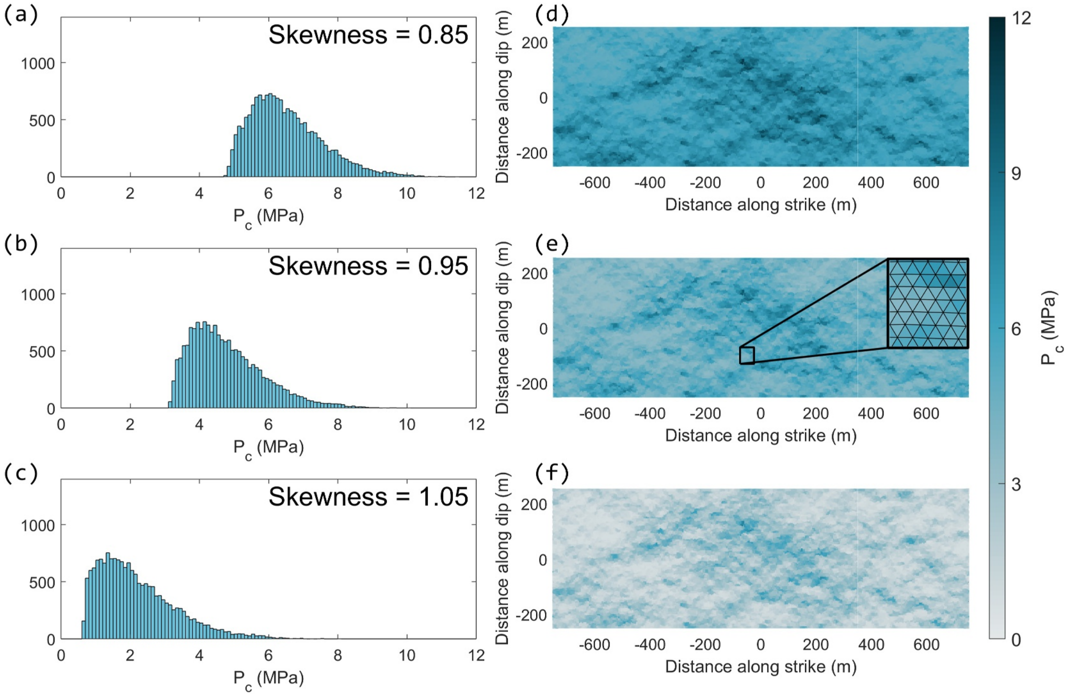

Figure 2. Histogram (left) and spatial distribution (right) of critical pressure P_c on a rough fault ($C = 0.5\%$) under (a, d) low, (b, e) medium and (c, f) high stress environments corresponding to $f_0 = 0.39$, 0.44, and 0.52, respectively. The inset in (e) shows a zoom-in view of the triangular mesh. Skewness values of P_c are indicated in the corresponding histogram panels.

2.2. Fault Geometry and Triangular Mesh

Fault roughness is a fundamental characteristic of natural faults and is a key feature of our model. Observations from field studies and laboratory experiments show that fault surfaces are commonly described by a self-affine relationship of the form

$$H = CL^{\zeta} \tag{9}$$

where H is the standard deviation of height fluctuations at length scale L with respect to a planar fault, C is the roughness amplitude at a reference length scale of 1 m and ζ is the Hurst exponent which describes how the amplitude of height fluctuations changes with scale (Brodsky et al., 2016; Candela et al., 2012; Power & Tullis, 1991). When $\zeta = 1$, the surface exhibits self-similar scaling, whereas values of $0 < \zeta < 1$ correspond to self-affine geometries typical of natural faults. Measurements from fault outcrops suggest that the roughness amplitude C lies within a narrow range, typically between 0.1% and 1%, while ζ generally falls between 0.6 and 0.8.

We consider a self-affine normal fault with length $a = 1500$ m and width $b = 500$ m, dipping at 70°. We adopt $\zeta = 0.8$, and consider three C values representative of faults ranging from relatively smooth to rough: 0.2%, 0.5%, and 0.8%. We generate self-affine rough faults using a spectral method (Candela et al., 2009) that prescribes the Fourier amplitude spectrum according to a given Hurst exponent and a random Fourier phase spectrum. By varying the random seeds of the stochastic phase generator, we produce several instances of rough fault surfaces with the same statistical properties. This enables a systematic exploration of how the spatial heterogeneity in fault geometry influences fault stresses, rupture dynamics and seismicity migration patterns.

To capture the geometric complexity of the rough faults, we discretize them using a triangular mesh (Zielke et al., 2017) generated by Delaunay triangulation (Figure 2b). Each triangle has a typical edge length of approximately 10 m (corresponding to an area of $\sim$44 m^2), which provides an appropriate balance between geometric resolution and computational efficiency. A relatively regular Delaunay mesh is used intentionally to avoid large variations in triangle size, ensuring that estimates of rupture area and event magnitude are controlled by fault roughness and stress conditions rather than mesh irregularity (Figure S2 in Supporting Information S1).

2.3. Fault Strength and Friction Law

Fault strength in our model is governed by the Mohr-Coulomb failure criterion: on a given fault patch, slip starts when the shear traction exceeds a frictional strength threshold given by $\mu_s(\sigma - p)$, where μ_s is the static friction coefficient, σ the resolved normal total stress onto the potential slip plane and p the pore pressure.

During slip, we assume an instantaneous weakening: the friction coefficient drops from its static value μ_s to a lower dynamic value μ_d. At the end of each rupture event, we assume instantaneous frictional healing: the friction coefficient returns to its static value immediately after slip stops. We also assume zero cohesion, so that failure is governed solely by frictional strength. This simplified friction law allows us to capture essential features of unstable slip behavior while maintaining computational efficiency in resolving the complexity of rough fault surfaces. To isolate the role of fault roughness as the sole source of heterogeneity in our model, the static and dynamic friction coefficients are kept constant in space and time.

2.4. Pre-Stress Distribution

The initial stress on the fault is determined by a depth-dependent background stress tensor caused by overburden and initial fluid pressure, which is commonly adopted in modeling studies of fluid injection (Cappa & Rutqvist, 2011; Rutqvist et al., 2002), to better represent realistic in situ stress conditions. We show that this assumption does not affect our main conclusions regarding the migration behavior of induced seismicity by showing that results of simulations with depth-dependent and uniform background stresses are similar in three representative cases with different values of roughness amplitude (see Text S1 in Supporting Information S1).

Since we consider a normal faulting regime, the maximum total principal stress is vertical and the minimum horizontal stress is perpendicular to the fault strike. The maximum principal stress increases with depth z as $\sigma_v = \rho_r g z$, where ρ_r is the rock density. The horizontal principal total stresses are defined by two parameters: the ratio between the minimum horizontal stress and the vertical stress $K_0 = \sigma_h/\sigma_v$, and the ratio between the minimum and maximum horizontal total stresses $K_h = \sigma_h/\sigma_H$. The horizontal stress ratios and their orientations are assumed constant in space and time. The initial Terzaghi effective stress tensor in the principal stress coordinate system is

$$\mathbf{\Sigma} = \begin{bmatrix} \sigma_h & 0 & 0 \\ 0 & \sigma_H & 0 \\ 0 & 0 & \sigma_v \end{bmatrix} - \rho_w g z \mathbf{I}_3 \tag{10}$$

where $\mathbf{I}_3$ is the identity matrix of size 3. On a fault patch with unit normal vector $\mathbf{n}$, the traction vector is $\mathbf{t} = \mathbf{\Sigma} \cdot \mathbf{n}$, the effective normal traction $\sigma' = \mathbf{t} \cdot \mathbf{n}$ (positive in compression), and the shear traction in the dip direction $\tau = (\mathbf{t} - \sigma' \mathbf{n}) \cdot \mathbf{d}$, where $\mathbf{d}$ is the unit vector in the dip direction (Jaeger et al., 2009). On a rough fault, the normal vector $\mathbf{n}$ has strong spatial variations and the smoothly depth-dependent background stress field assumed here results in a spatially heterogeneous pre-stress distribution along the fault.

To quantify how close to criticality each fault patch is, we define the *critical pressure* P_c as the increment of pore pressure (relative to its initial value) required to reach criticality by satisfying $\tau_0 = \mu_s(\sigma_0' - P_c)$, where σ_0' is the initial effective normal traction and τ_0 the initial shear traction on the fault patch. That is:

$$P_c = \sigma_0' - \frac{\tau_0}{\mu_s}. \tag{11}$$

A lower P_c implies that the fault patch is more critical, that is, it requires less additional pressure to rupture. Since σ_0' and τ_0 vary spatially due to fault roughness, the distribution of P_c is also heterogeneous across the fault.

For a given fault roughness, the degree of fault criticality is primarily controlled by the stress ratio K_0. To provide a more intuitive measure relevant for fault slip, we define f_0 as the ratio of shear to normal stress on the reference

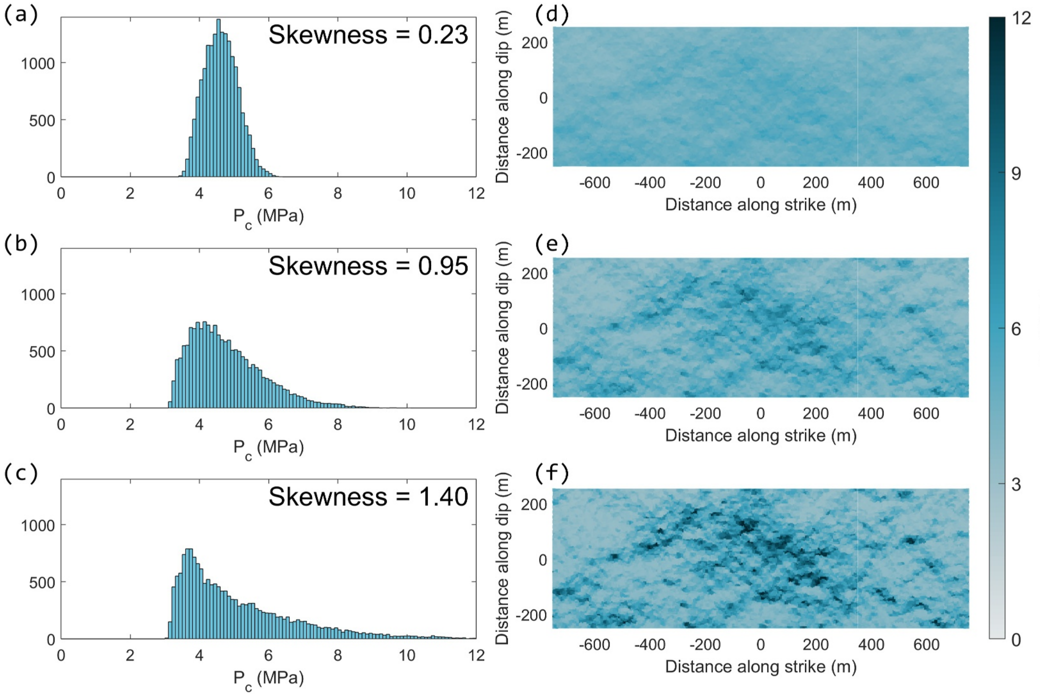

Figure 3. Histogram (left) and spatial distribution (right) of critical pressure P_c on three faults with (a, d) low, (b, e) medium and (c, f) high values of fault roughness amplitude C but same random seed and background stress. Skewness values of P_c are indicated in the corresponding histogram panels.

planar fault with the same background stress ratio (K_0 and K_h) as the modeled rough fault. Figure 2 shows examples of the spatial distribution of P_c on a same fault at three different values of stress ratio $K_0 = 0.65, 0.63$, and 0.60, which correspond to $f_0 = 0.39$, 0.44, and 0.52, representing low, medium and high stress environments, respectively. These values are chosen to ensure that, prior to injection, all fault patches are stressed below failure, while still being sufficiently close to criticality to initiate multiple rupture events during the injection period. The examples illustrate that a higher f_0 results in a more critical fault with a more positively skewed statistical distribution of P_c, as expected from previous literature (Maurer, 2024).

We find that the roughness amplitude C also plays a key role in shaping the statistical properties of P_c. Figure 3 shows the spatial distribution of P_c for three faults with different values of C but the same random seed and f_0. Smoother faults (low C) tend to produce an approximately normal distribution of P_c, while rougher faults lead to wider and highly skewed distributions with long tails toward high P_c values. This trend is consistent with previous derivations (Maurer, 2024) and also holds for a depth-independent background stress tensor (Figure S3 in Supporting Information S1), highlighting the non-trivial influence of the self-affine fault roughness in controlling the pre-stress distribution.

2.5. Rupture Sequences and Stress Redistribution

As fluid pressure increases due to injection, the effective normal stress on the fault and thus the fault strength are reduced. A rupture is triggered when the static frictional strength on a fault patch reaches its shear stress. Then, the patch undergoes an instantaneous strength drop, by which its friction coefficient drops from its static value of $\mu_s = 0.6$ to a dynamic value of $\mu_d = 0.55$, resulting in a stress drop and slip on this patch. The resulting slip redistributes stresses across the fault via static elastic interactions. Any patches that are brought to criticality by this stress redistribution are assumed to rupture as part of the same event. The cascading process of slip, stress transfer and criticality is iterated until no more fault patch is at criticality. During the iterations, the rupture patches remain at their dynamic friction strength and heal back to the static friction strength after the slip stops for each rupture event. The resulting set of ruptured patches forms the earthquake rupture area. The event magnitude is computed by integrating the final slip over the rupture area. At the end of the event, fault strength is immediately restored to its static level. With continued fluid injection, this process repeats, generating a series of rupture events.

To calculate the stress redistribution, we adopt the boundary element method based on the elastic Green's functions for triangular dislocations in an elastic half-space by Nikkhoo and Walter (2015). The Green's functions are the static elastic stress changes received on each triangular fault patch induced by a unit slip on each fault patch, considering their orientations. These are pre-computed and stored in influence matrices K_τ and K_σ associated with shear and normal stress changes, respectively. Our choice of model parameters, including the element size and criticality of the fault, prevents tensile stresses (i.e., normal stress dropping to zero) during the entire simulation.

The procedure for each rupture event is summarized by the following pseudo-code, which is repeated until the end of the simulation:

1. On each fault patch, calculate the next rupture time owing to pressure evolution only (no additional slip) by solving for t the equation

$$p(t) = \sigma - \frac{\tau}{\mu_s} \tag{12}$$

   where $p(t)$ is given analytically by Equation 7 and σ and τ are fixed to their previous values. We solve this equation numerically with a tolerance of 2.2×10^{-16} seconds. Then find the earliest rupture time t_i among all fault patches.
2. Update pore pressure on all fault patches at time t_i.
3. While slipping patches that satisfy $\tau \geq \mu_s(\sigma - p)$ exist
    (a) Calculate $\Delta\tau'$ on the slipping patches

$$\Delta\tau' = \mu_d(\sigma - p) - \tau \tag{13}$$

    (b) Compute slip increment of the slipping patches due to $\Delta\tau'$ (see Text S2 in Supporting Information S1 for detail derivation)

$$D = \left(K_\tau - \mu_d K_\sigma\right)^{-1} \Delta\tau' \tag{14}$$

    (c) Update $\sigma = \sigma + K_\sigma D$ and $\tau = \tau + K_\tau D$ on all fault patches accounting for stress transferred by slip.
4. Calculate the rupture area A (total area of all slipping patches), average of slip $\bar{D}$, and magnitude

$$M = \frac{2}{3}\log_{10}\left(\mu A \bar{D}\right) - 6.07 \tag{15}$$

   of the rupture event.

3. Seismicity Front Migration Without Stress Interactions

Before studying the complete problem through simulations, in this section we develop analytical insights on simpler problems in which the stress interactions between fault patches due to slip are ignored. In this framework, the rupture area of each event is assumed to be much smaller than the characteristic size of a fault patch, so that elastic stress transfer to neighboring patches is negligible. In these cases, fault patches rupture in isolation, producing a local stress drop in the broken patch but without transferring stresses to other patches. This is applicable to discontinuous fault systems composed of many small, mechanically isolated segments, for which earthquakes can be approximated as non-interacting point sources (Segall & Lu, 2015). The results presented in this section will serve as a reference to interpret the results of simulations with stress interactions in Section 4.

3.1. Homogeneous Initial Stress

Here, we establish a theoretical prediction of seismicity migration on a planar fault with spatially uniform initial stress and ignoring elastic stress interactions. In this simplified scenario, the critical pressure P_c is uniform and rupture nucleation is solely governed by the evolution of pore pressure due to fluid injection. Under these assumptions, the seismicity front is obtained by finding the along-fault radial distance from the injection (r) at which pore pressure reaches the critical pressure:

$$P_c = \Delta p(r,t) = P_v E_1\left(\frac{r^2}{4D_0 t}\right) \tag{16}$$

The resulting seismicity front distance takes the form of a diffusive front:

$$r = \sqrt{4Dt} \tag{17}$$

where

$$D = E_1^{-1}\left(\frac{P_c}{P_v}\right) D_0 \tag{18}$$

is the *apparent diffusivity* that would be inferred from a seismicity catalog by the common practice of fitting the diffusion-like Equation 17 to the seismicity front (Shapiro et al., 2002). Note that P_c/P_v is identical to the fault stress parameter $T = \left(1 - \frac{\tau_0}{\mu_s \sigma_0'}\right)\frac{\sigma_0'}{P_v}$ introduced by Bhattacharya and Viesca (2019) in a model with constant friction and later extended to include frictional weakening (Sáez & Lecampion, 2024), as in our model. If $P_c/P_v > 1$, that is, if the fault is far from criticality or the characteristic pressure is low, the function E_1 can be approximated by an exponential function (Dake, 1978), leading to the following simplified expression:

$$D \approx \exp\left(-\frac{P_c}{P_v} - \gamma\right) D_0 \tag{19}$$

where γ is Euler's constant, and $\exp(-\gamma) \approx 0.5615$. Equations 18 and 19 show that the apparent diffusivity D depends not only on the hydraulic diffusivity D_0 but also on mechanical factors such as the critical pressure P_c. For a given characteristic pressure, a higher critical pressure will cause a lower D.

To validate the theoretical prediction, we simulate a planar fault with uniform initial effective normal stress of 20 MPa and shear stress of 9 MPa, therefore $P_c = 5$ MPa. Other parameter values are indicated in Table 1, including $\beta = 10^{-8}$ 1/Pa, $D_0 = 1$ m^2/s and $P_v = 796$ kPa. Stress interactions between fault patches are disabled, ensuring that ruptures are solely driven by pore pressure changes. Figure 4 shows that the simulated seismicity front follows the 5 MPa pore pressure contour, as expected. By fitting it to Equation 17, we obtain an apparent diffusivity $D = 0.001$ m^2/s, which is consistent with the value obtained from Equation 19.

Seismicity occurring behind the seismicity front in Figure 4 organizes along multiple fronts that also closely follow pressure contours. These secondary fronts result from the reactivation of the same fault patches after their initial rupture. The pressure contour associated with each front corresponds to the additional pressure needed for the static strength to reach the reduced shear stress after the previous stress drop. For example, after the first rupture at a pressure of 5 MPa, the shear stress τ of all fault patches drops to $\mu_d(\sigma_0' - 5) = \mu_d(20 - 5) = 8.25$ MPa; the next rupture will then occur when pressure reaches $\sigma_0' - \tau/\mu_s = 20 - 8.25/0.6 = 6.25$ MPa; and so on for successive fronts. This stepwise reactivation produces a series of separate seismicity fronts that closely match the corresponding pressure contours.

The foregoing example illustrates that the apparent diffusivity can be orders of magnitude lower than the hydraulic diffusivity, indicating that the seismicity front propagates more slowly than the *nominal pressure front* defined by $r = \sqrt{4D_0 t}$. Based on Equation 18, the nominal pressure front corresponds to a pore pressure change contour of approximately $0.2P_v$, as derived from $P_c/P_v = E(1) \approx 0.2$. In our cases, this contour corresponds to a pressure change of about 0.18 MPa. Figure 4 illustrates that the nominal pressure front migrates much faster than the seismicity front, highlighting that fault criticality has a crucial effect on the migration speed of induced seismicity. This should be taken into account when interpreting the apparent diffusivities estimated from the spatio-temporal distribution of seismic catalogs.

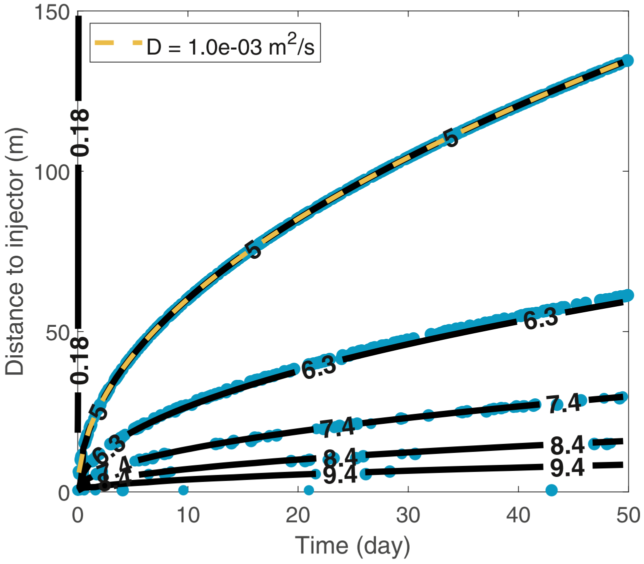

Figure 4. Spatio-temporal evolution of injection-induced seismicity (blue circles) on a planar fault with uniform P_c of 5 MPa, ignoring stress interactions. Yellow dashed curve is the best-fitting square root function with an apparent diffusivity D of 0.001 m^2/s. Black curves are contours of pore pressure (values indicated by labels in MPa) that theoretically match the primary and secondary seismicity fronts.

To further examine the relationship between apparent and hydraulic diffusivities, D and D_0, we compare the ratio D/D_0 obtained from simulations with different uniform initial stresses, which is similar to the squared amplification factor λ^2 in Bhattacharya and Viesca (2019) and from Equation 18 for different P_c/P_v values (Figure 5). The results demonstrate that D can be either higher or lower than D_0, depending on the initial stress environment. Specifically, cases with $P_c/P_v < 0.2$ exhibit $D > D_0$, in agreement with Equation 18. The simulation results closely follow this theoretical relationship, while the approximation given by Equation 19 begins to deviate for $P_c/P_v < 1$. These results show that low critical pressure P_c relative to the characteristic pressure P_v is a necessary condition for observing seismicity fronts that outpace the nominal pressure front. In the next section, we extend this analysis to more realistic models with heterogeneous initial stress due to fault roughness. In Section 5, we will examine how stress heterogeneity affects the ratio D/D_0, and whether conditions for $D > D_0$ are physically plausible.

3.2. Heterogeneous Initial Stress

Here, we develop a probabilistic prediction of the seismicity front evolution on a rough fault with heterogeneous initial stresses arising from fault roughness, and again ignoring stress interactions.

We begin by assuming that the distribution of P_c is spatially independent (non correlated). The probability density function of P_c is spatially uniform across the fault, and we approximate it by the statistical histogram of P_c (Figure 2). For each time bin t (in 5-day intervals) and radial distance bin r (in 1-m bins), we compute the probability density $\mathbb{P}_p$ of P_c being equal to the pore pressure change $\Delta p(r,t)$:

$$\mathbb{P}_p(r,t) = \mathbb{P}(P_c = \Delta p(r,t)) \tag{20}$$

To account for the geometric effect, we compute the area dA_r of the intersection between the rectangular fault and a ring of radial width dr at a distance r from the injection well:

$$dA_r(r) = \begin{cases} 2\pi r dr & r \leq b/2 \\ 4r \arcsin\left(\dfrac{b}{2r}\right) dr & b/2 < r \leq a/2 \\ \left(2\pi r - 4r \arccos\left(\dfrac{b}{2r}\right) - 4r \arccos\left(\dfrac{a}{2r}\right)\right) dr & a/2 < r \leq \sqrt{a^2 + b^2} \end{cases} \tag{21}$$

On each given time window, the area-weighted criticality probability $\mathbb{P}_A = \mathbb{P}_p \cdot dA_r$ is integrated from the injector to a given distance r and normalized by the value of the integral at the maximum distance to obtain the probability that P_c is reached at a distance $\leq r$ (Figure 6). This provides a probabilistic prediction of the position of the seismicity front.

Considering the heterogeneity in initial stress, we define the seismicity front as the collection of rupture events whose distance falls between the 80th and 95th percentiles of hypocenter distances within a 5-day sliding window (Danré et al., 2024). Therefore, to predict the seismicity front, we extract the area bounded by the 0.8 and 0.95 contours of the integral of $\mathbb{P}_A$. Figure 6c presents this predicted seismicity front. It exhibits a diffusion-like behavior,

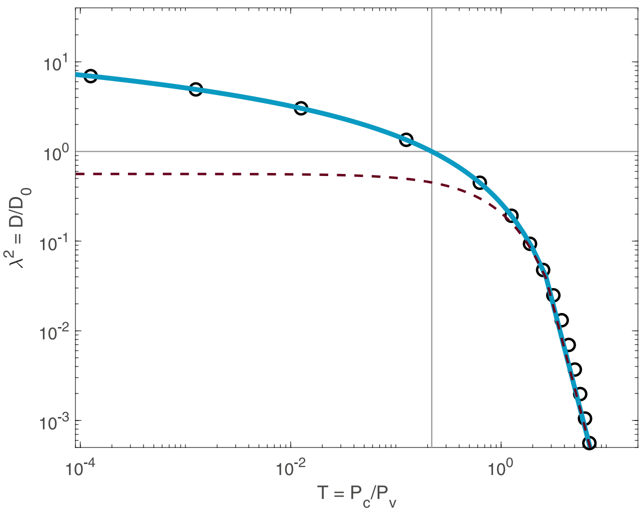

Figure 5. Ratio of apparent to hydraulic diffusivities D/D_0 as a function of normalized critical pressure P_c/P_v in models with uniform initial stress on a planar fault ignoring stress interactions. Circles denote the simulation results. Blue solid curve shows the theoretical relationship given by Equation 18, red dashed curve is its approximation by Equation 19. Gray solid line denotes $D = D_0$ and its corresponding $P_c/P_v \approx 0.2$.

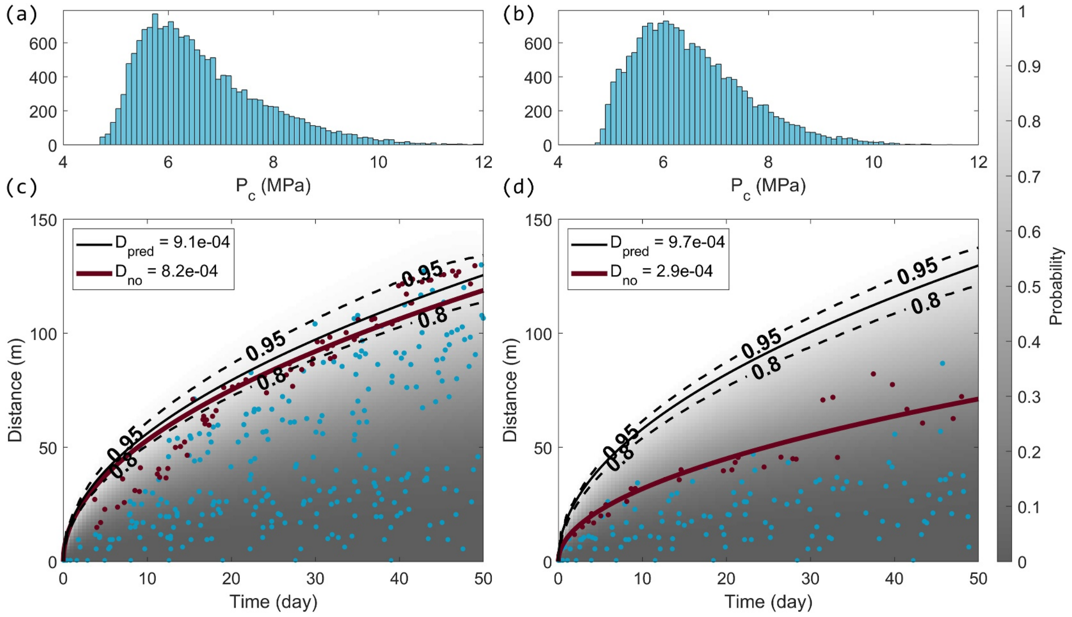

Figure 6. (a, b) P_c distributions for two fault models generated with the same roughness amplitude C but different random seeds. (c, d) Prediction of seismicity front without stress interactions (black solid curve). Background color and black dashed lines show the integral of $\mathbb{P}_A$ and its contours at 0.8 and 0.95. Blue circles denote seismicity simulated without stress interactions. Dark red circles are events defining the seismicity front. Red curve is the best-fitting square root function to the seismicity front.

with the predicted apparent diffusivity of $D_{pred} = 9.2 \times 10^{-4}$ m^2/s. This value closely aligns with the apparent diffusivity $D_{no} = 8.2 \times 10^{-4}$ m^2/s derived from the seismicity catalog simulated without stress interactions (subscript no indicates no stress interactions), suggesting that a first-order prediction of seismicity front migration is achievable from statistical stress conditions and pore pressure evolution.

While our basic predictions based on a spatially independent distribution of P_c generally capture the overall migration trend of the simulated seismicity, notable deviations are observed in certain cases. Figure 6 shows results of two simulations with similar statistical distributions of P_c but exhibiting distinct seismicity front evolution. This discrepancy suggests that, beyond the statistical distribution, the spatial arrangement of critical and non-critical patches plays a key role in controlling rupture propagation. To account for this effect, we extend our prediction framework to incorporate spatially dependent P_c. Using the same example shown in Figure 6, we estimate the local P_c distribution every 50 m across the fault. We then recompute the pressure probability density $\mathbb{P}_p$ for each distance and time bin based on these localized distributions. As shown in Figure 7, incorporating spatial dependence significantly improves the prediction and brings it into better agreement with the simulated

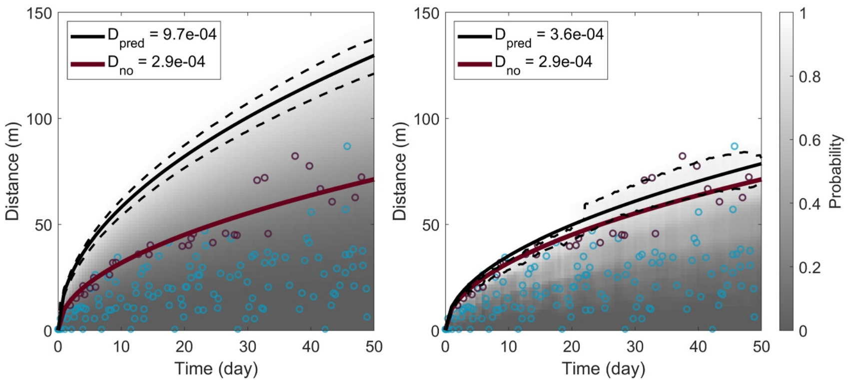

Figure 7. Prediction of seismicity front from (left) spatially independent and (right) spatially dependent P_c distributions.

seismicity front. This result demonstrates the importance of spatial heterogeneity in fault strength and highlights how the spatial arrangement of critical patches governs the spatio-temporal evolution of injection-induced seismicity.

3.3. Effect of Roughness and Initial Stress Environment

To investigate how roughness and initial stress environment affect seismicity migration, we simulate fault models with three different C values and three different f_0 values. The corresponding distributions of P_c are shown in Figures 2 and 3. As illustrated in Figure 8, seismicity migrates faster on rougher faults and in higher initial stress environments since they have more patches that are close to criticality. As a result, rupture events are triggered earlier, leading to faster migration and therefore, higher apparent diffusivity. This emphasizes the critical role of both fault roughness and stress environment in shaping the spatio-temporal evolution of induced seismicity.

As demonstrated in Section 3.2, the spatial arrangement of critical patches, controlled by the random seed used to generate the self-affine rough fault, affects seismicity migration. To systematically capture the general trends across different fault roughness amplitudes and initial stress environments, we perform similar simulations using 30 different random seeds for each C and f_0, which generate comparable statistical distributions of P_c but different spatial arrangements (Figure S6 in Supporting Information S1), and compare their resulting apparent diffusivities. Figure 9 presents histograms of apparent diffusivity for each C and f_0. Despite variability introduced by the spatial arrangement of critical patches, the overall pattern remains consistent with that shown in Figure 8. Seismicity tends to migrate more rapidly on rougher faults and in higher stress environments. This phenomenon persists with different hydraulic diffusivities (Figure S7 in Supporting Information S1). These results reinforce the conclusion that both fault geometry and initial stress environment play a dominant role in controlling the rate of seismicity migration, even when accounting for variabilities induced by the spatial arrangement of the fault roughness.

4. Seismicity Front Migration With Stress Interactions

To evaluate the role of stress interactions in controlling seismicity front migration, we incorporate static stress transfer between fault patches into the simulations. In contrast to the previous section (Figure 8), where rupture events are driven solely by direct pore pressure changes, considering stress interactions allows for rupture-induced stress changes to influence neighboring patches. As a result, rupture events can grow larger in magnitude and break a larger area. We perform simulations using the same model parameters as in Figure 8, with the only difference being the consideration of stress interactions. The simulated spatio-temporal evolution of seismicity and the calculated apparent diffusivity, shown in Figure 10, demonstrate that seismicity still migrates faster on rougher faults and in higher initial stress environments, as in Figure 8. However, the contrast in apparent diffusivity among different roughness amplitudes becomes less distinct when stress interactions are considered. Across all cases, the apparent diffusivities are generally higher than in the corresponding simulations without stress interactions. This highlights the accelerating effect of stress transfer, promoting faster seismicity migration.

To ensure the robustness of our results, we perform the same simulations with different random seeds as in Figure 9, taking stress interactions into account. The statistical distributions of apparent diffusivity obtained from these simulations are presented in Figure 11. While variability persists due to differences in the spatial arrangements of critical patches, the overall trends remain consistent. Seismicity generally migrates faster on rougher faults and in higher stress environments. However, the differences in D between different roughness amplitudes are significantly reduced when stress interactions are included. This could be explained by the additional slip-induced shear resistance caused by fault roughness, known as roughness drag (Dieterich & Smith, 2009; Fang & Dunham, 2013). Roughness drag is larger on rougher faults and tends to stabilize slip (Ozawa et al., 2019; Tal et al., 2018). Therefore, we expect it to compete against the accelerating effect of stress interactions on seismicity migration, thus narrowing the difference in migration speeds between smoother and rougher faults.

To further quantify the impact of stress interactions on seismicity migration, we compute the ratio of apparent diffusivity D between simulations with and without stress interactions D/D_{no} for each model. As illustrated by the statistical distributions shown in Figure 12, the ratios are dominantly greater than one, indicating that stress interactions often accelerate seismicity migration. These comparisons reveal that the acceleration of seismicity migration due to stress interactions is greater on smooth faults, as indicated by higher D/D_{no} ratios. On the contrary, the effect of stress interactions on rough faults is more subtle. This difference in the efficiency of stress

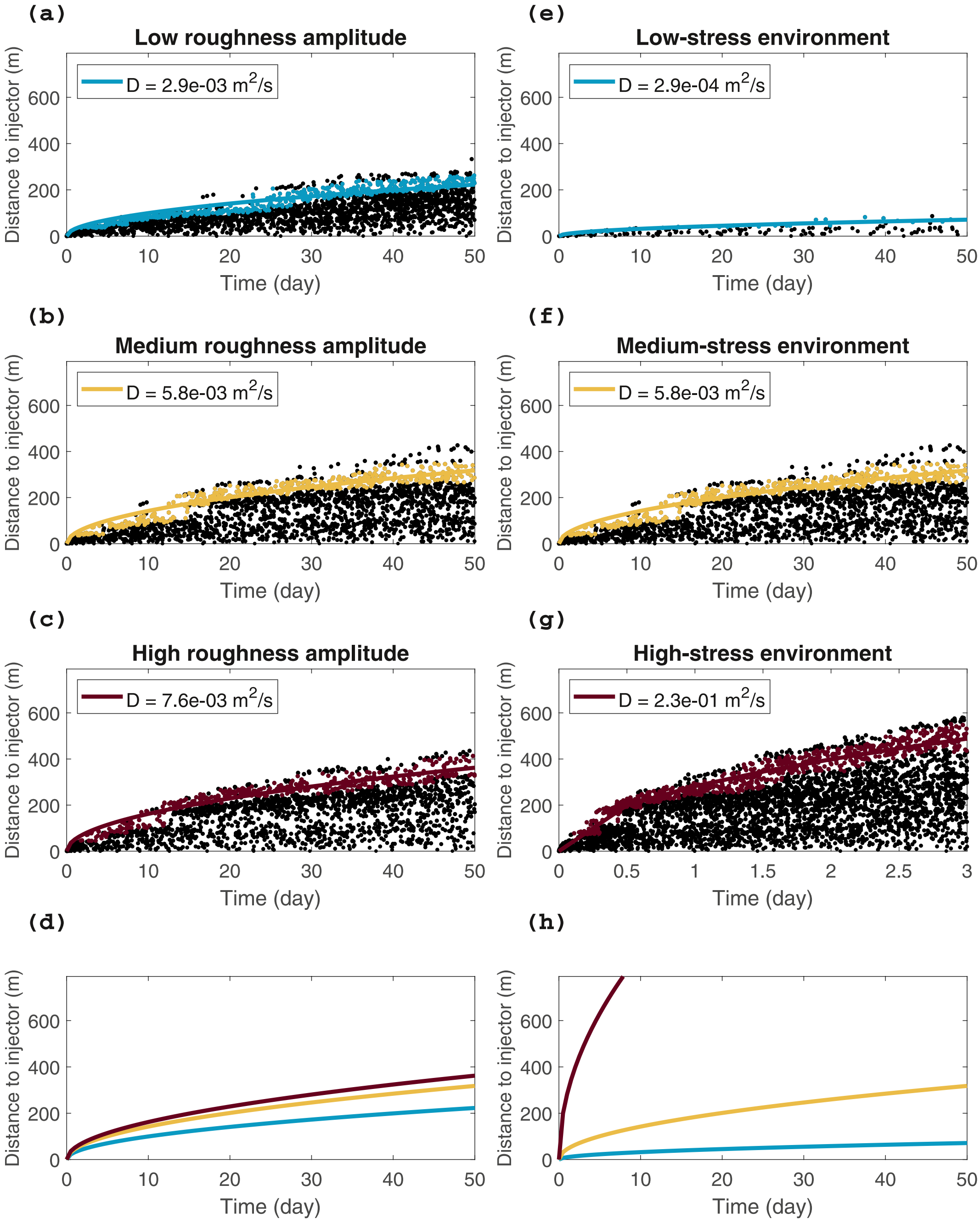

Figure 8. Spatio-temporal evolution of seismicity at (a) low (b, e–g) medium and (c) high roughness amplitudes in (e) low (f, a–c) medium and (g) high stress environments in models without stress interactions. Black circles indicate the location (distance to injector) and occurrence time of earthquakes. Colored circles and curves correspond to the seismicity front and the best-fitting square root function. (d) Comparison of the fitted seismicity front with the corresponding colors in (a–c) for different roughness amplitudes. (h) Comparison of the fitted seismicity front with the corresponding colors in (e–g) for different initial stress environments.

interactions between smooth and rough faults can potentially be explained by the roughness drag which leads to an additional shear resistance (Fang & Dunham, 2013). As for different initial stress environments, the ranges of D/D_{no} are nearly identical, which is expected given that the geometric orientation of the fault patches remains unchanged. These results highlight the role of stress interactions in accelerating seismicity migration.

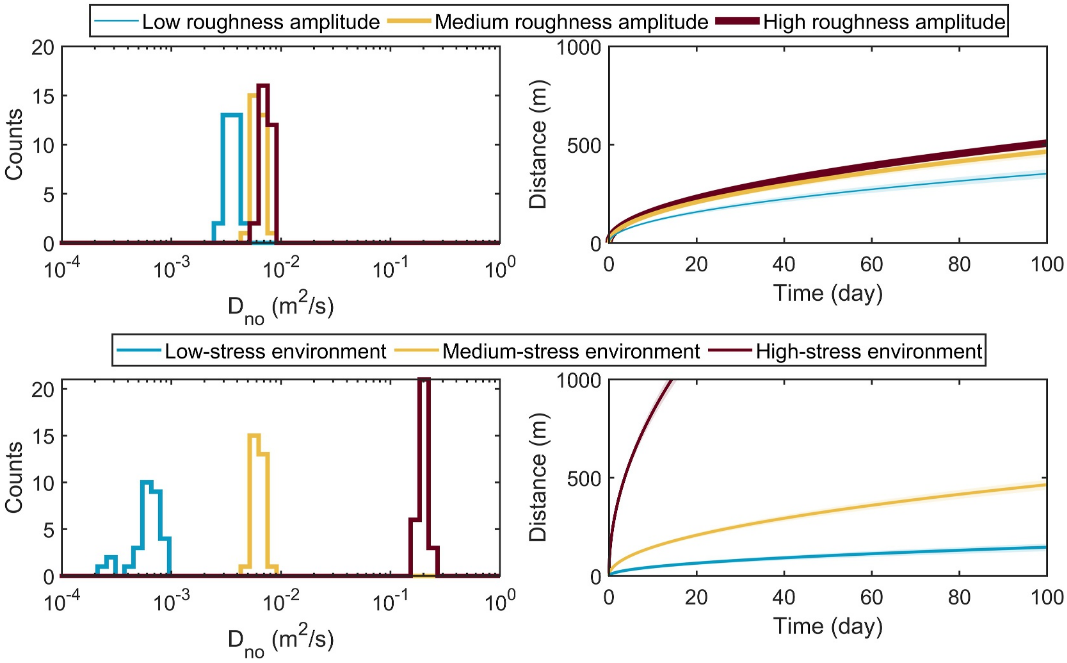

Figure 9. (left) Histograms of the apparent diffusivity of the seismicity front for sets of 90 simulations without stress interactions at 3 roughness amplitudes (top) and 3 initial stress environments (bottom). (right) Comparison of the fitted seismicity front associated with the mean values of apparent diffusivity for different roughness amplitudes (top) and initial stress environments (bottom). The shaded areas represent the standard deviation of apparent diffusivity for each case.

While fault roughness and initial stress environment primarily govern the distribution of pre-stress, and hence set the baseline conditions for rupture nucleation, the inclusion of stress interactions introduces an additional layer of complexity. The interplay between stress interactions and fault roughness reveals a trade-off that can significantly alter the migration speed. As shown in the previous section, rougher faults tend to have faster seismicity migration due to a larger proportion of critical fault patches. Yet, the acceleration of seismicity migration due to stress transfer is reduced by roughness drag (Fang & Dunham, 2013).

5. Relationship Between Apparent Diffusivity and Hydraulic Diffusivity Along a Rough Fault

Here we show, based on our model, that on natural rough faults the apparent diffusivity D inferred from seismicity migration is most often smaller than the hydraulic diffusivity D_0.

Since E_1 is a decreasing function, Equation 18 and Figure 5 show that $D > D_0$ if

$$\frac{P_c}{P_v} < E_1(1) \approx 0.2 \tag{22}$$

In models with uniform initial stress, P_c can be arbitrarily low, making it theoretically possible to observe $D > D_0$ by having a P_c/P_v lower than 0.2. However, in more realistic models incorporating fault roughness, P_c is spatially heterogeneous, and achieving a low P_c over a large area of the fault is unlikely. To show this, we first consider the constraints imposed by injection conditions. Specifically, to avoid tensile fracturing, the maximum pore pressure change throughout the simulation must not exceed the initial effective normal stress:

$$\Delta p(r,t) = P_v E_1\left(\frac{r^2}{4D_0 t}\right) < \sigma_0' \tag{23}$$

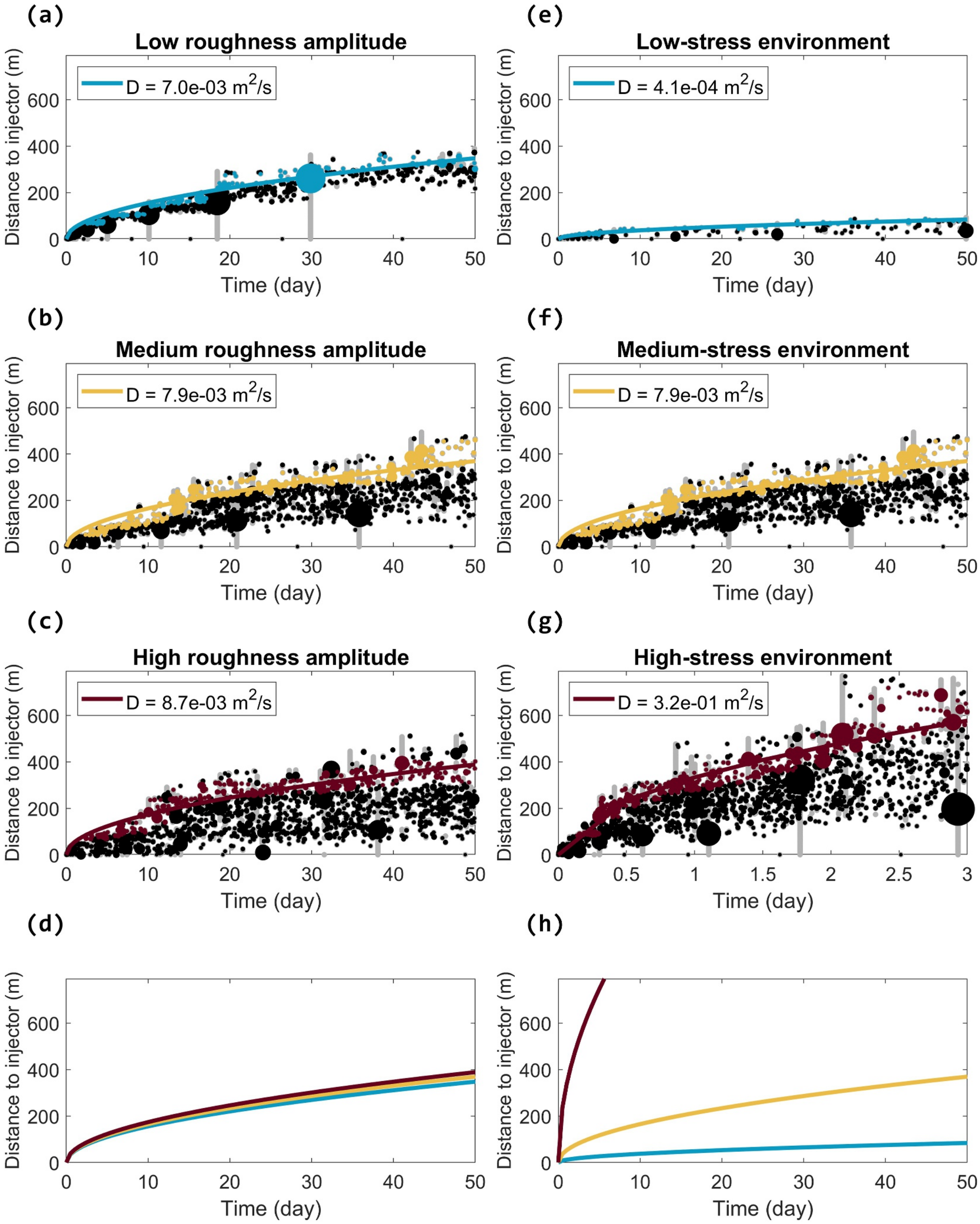

Figure 10. Spatio-temporal evolution of seismicity at (a) low (b, e–g) medium and (c) high roughness amplitudes in (e) low (f, a–c) medium and (g) high stress environments in models with stress interactions. Black circles indicate the location (distance to injector) and occurrence time of earthquakes, sized-coded by magnitude. Colored circles and curves correspond to the seismicity front and the best-fitting square root function. Gray bars show the rupture area of each event. (d) Comparison of the fitted seismicity front with the corresponding colors in (a–c) for different roughness amplitudes. (h) Comparison of the fitted seismicity front with the corresponding colors in (e–g) for different initial stress environments.

Typically, the nominal pressure front $r_p = \sqrt{4D_0 t}$ is far from the borehole at the end of injection. A typical seismicity cloud extends over distances of at least 100 m, so we assume a pressure front radius $r_p \geq 100$ m. Given r_b is about 0.1 m, this corresponds to $r_p/r_b \geq 10^3$. The maximum pressure change occurring at the borehole is $P_v E_1\left((r_b/r_p)^2\right) \approx 10P_v$. For a significantly more distant pressure front of $r_p = 10^5 r_b$, the maximum pressure is

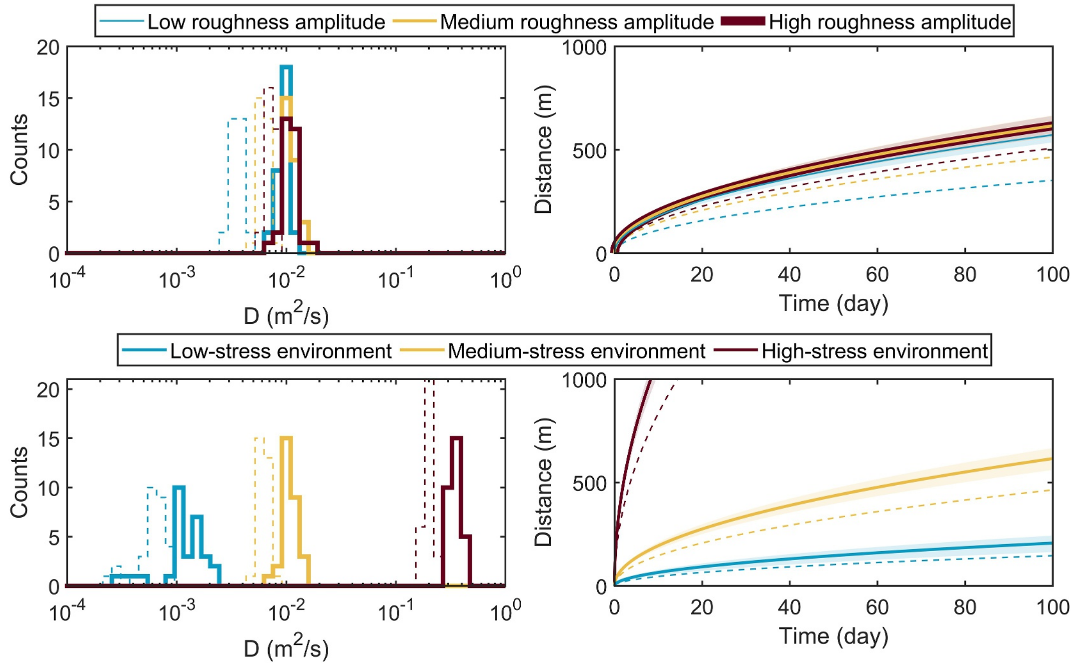

Figure 11. (left) Histograms of the apparent diffusivity of the seismicity front for sets of 90 simulations with stress interactions at 3 roughness amplitudes (top) and 3 initial stress environments (bottom). (right) Comparison of the fitted seismicity front (solid lines) associated with the mean values of apparent diffusivity for different roughness amplitudes (top) and initial stress environments (bottom). Shaded areas represent the standard deviation of apparent diffusivity for each case. Dashed histograms and lines depict the results from simulations without stress interactions, as shown in Figure 9.

$P_v E_1(10^{-10}) \approx 20P_v$. This still remains within one order of magnitude of P_v, owing to the slow asymptotic behavior of the function E_1. Hence, substituting into Equation 23 yields

$$\frac{P_v}{\sigma_0'} < 0.1 \tag{24}$$

Combining Equations 22 and 24, the condition for $D > D_0$ becomes

$$P_c < 0.02\sigma_0' \tag{25}$$

To assess how often this condition is satisfied, we systematically examine the scenarios across wide ranges of C and f_0. While the observations suggest expected ranges of C between 0.1% and 1% (Section 2.2), we extend the range down to 0.01% to include unrealistically smooth faults for comparison. To explore the most favorable conditions for $D > D_0$, we vary f_0 to represent different critical stress environments. As shown in Figure 3, increasing C makes the P_c distribution more skewed. Meanwhile increasing f_0 shifts the entire P_c distribution closer to criticality and makes it slightly more skewed.

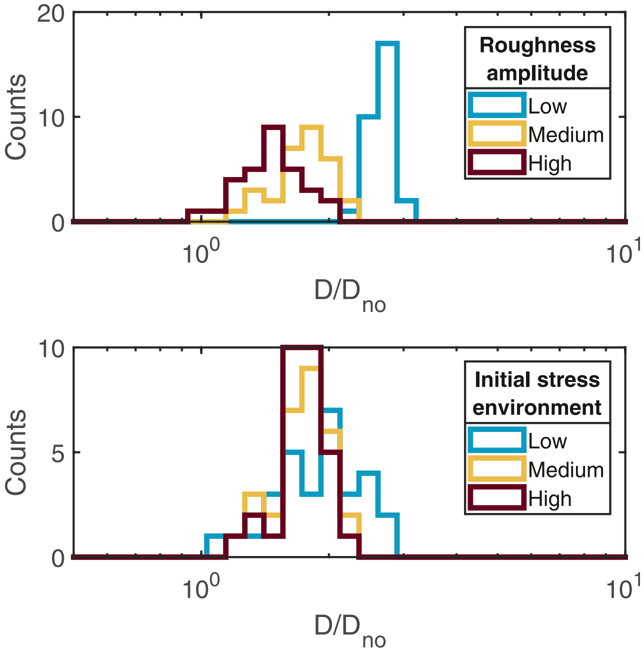

Figure 12. Ratio of apparent diffusivity D between with and without stress interactions (D/D_{no}) for different roughness amplitudes (top) and initial stress environments (bottom).

We uniformly sample 100 values of C from 0.01% to 1%, and 125 values of f_0 from 0.52 to 0.60. For each combination of C and f_0, we generate a random rough fault and compute its P_c distribution. If the fault is already critical prior to injection (i.e., at least one patch exceeds criticality before injection), we classify it as "initially critical" and exclude it. For subcritical faults (all patches below criticality), based on our definition of seismicity front, we define the representative P_c of a fault as the 20th percentile of the P_c values among ruptured patches where the local pore pressure change exceeds the

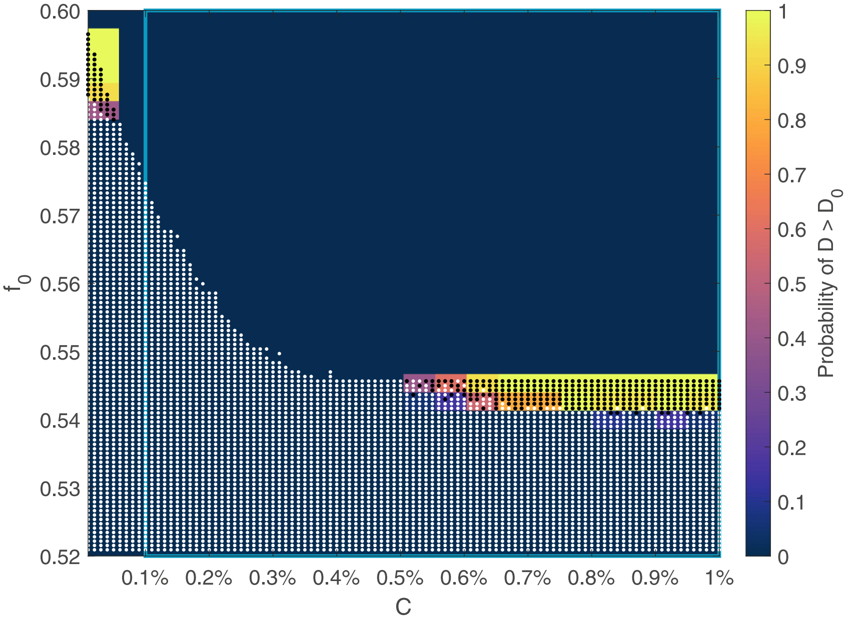

Figure 13. Probability of $D > D_0$. (Background color). Black dot denotes scenario with $D > D_0$. White dot denotes scenario with $D \leq D_0$. Cerulean rectangle denotes the realistic range of C.

local P_c by the end of injection. If the representative P_c satisfies Equation 25, we consider this case to meet the condition for $D > D_0$. The uniformly sampled 2-dimensional space (C, f_0) is further divided into a 20 × 35 grid, and the probability of $D > D_0$ is computed as the ratio of the number of cases that meet the condition to the total number of cases in each grid cell.

Figure 13 presents the probability of $D > D_0$ for different C and f_0. For extremely smooth faults (e.g., $C < 0.05\%$), the standard deviation of the P_c distribution is small, allowing for very high f_0 and hence high probabilities of $D > D_0$. However, for more realistic roughness amplitudes ($0.1\% \leq C \leq 1\%$), rougher faults are more likely to produce higher D. Indeed, the probability of observing $D > D_0$ becomes significant only when f_0 is pushed to its highest value. Building on the probability estimates shown in Figure 13, in Figure 14 we compare the inferred values of D/D_0 and P_c/P_v across all critical scenarios in Figure 13 with relatively high f_0 ($f_0 > 0.52$), as well as those simulations presented earlier in Sections 3 and 4 with $f_0 = 0.39$, 0.44, and 0.52. For the cases in Figure 13, D/D_0 is inferred from Equation 18 based on their representative values of P_c/P_v. The same method is used to estimate a representative P_c for the earlier simulations with realistic $C = 0.2\%$, 0.5%, and 0.8%; and $f_0 = 0.39$, 0.44, and 0.52. Yet, the apparent diffusivity D is obtained by fitting a square root function to the simulated seismicity front, as described in Sections 3 and 4. The comparison demonstrates that if the fault is very close to criticality (i.e., high f_0), unrealistic low C and higher C can lead to reduced P_c/P_v, and consequently higher D/D_0 (Figure 15). However, most cases remain above the threshold P_c/P_v of 0.2 (Figure 14), indicating that $D > D_0$ is only possible in cases with extremely critical initial stress conditions (Figure S8 in Supporting Information S1).

Figures 14 and 15 also include simulations accounting for static stress interactions. These show that the apparent diffusivity is consistently higher when stress interactions are included, relative to the cases without stress interactions with comparable initial conditions. We further compare our results with the relationship between $\lambda^2 = D/D_0$ and $T = P_c/P_v$ derived for circular ruptures by Sáez et al. (2022), which takes stress transfer into account but assumes constant friction, and find that our results are in good agreement if we set their constant friction coefficient equal to our static friction. These results suggest that while low P_c/P_v is a necessary condition for $D > D_0$, stress interactions can accelerate seismicity migration, therefore increase the potential for the seismicity front to outpace the nominal pressure front (Bhattacharya & Viesca, 2019; Sáez et al., 2022). Additionally, Figure 14 shows that, in our model, the effect of stress interactions is small compared to the effect of P_c/P_v, thus separating the two factors in real observations will be a challenge.

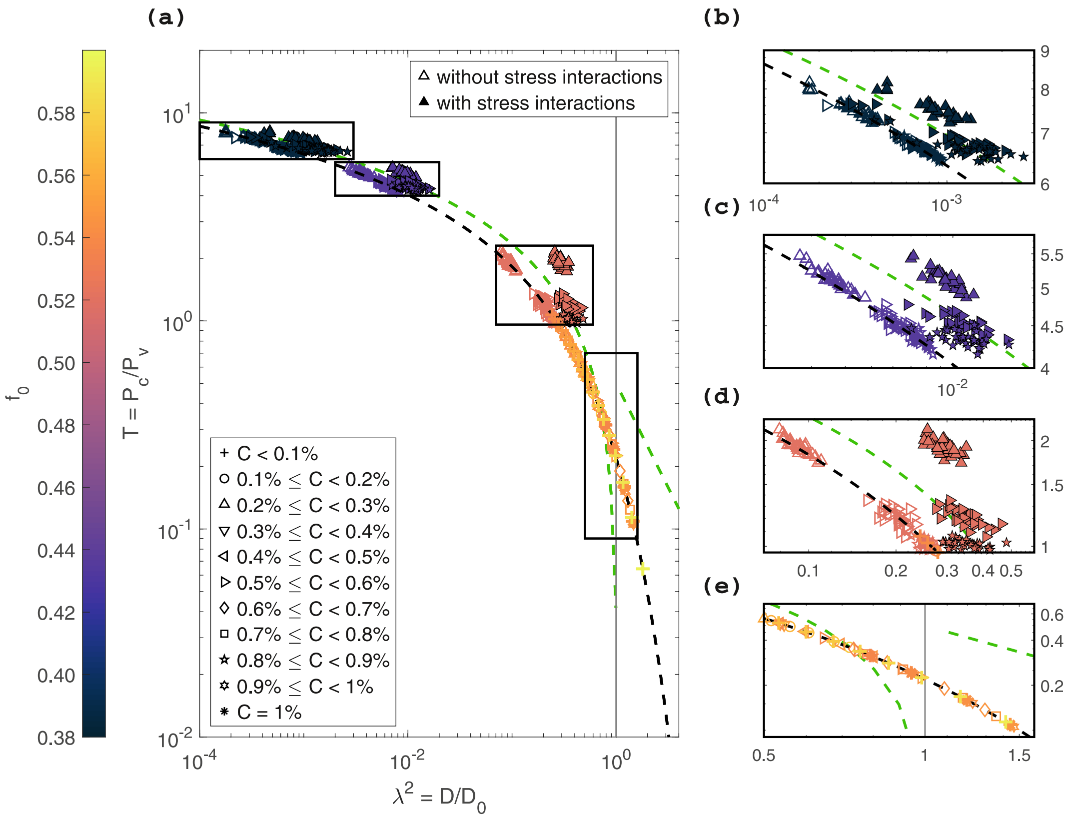

Figure 14. (a) Relationship between D/D_0 and P_c/P_v from simulations with heterogeneous initial stress, with stress interactions (filled symbols) and without stress interactions (empty symbols). Black dashed curve is the theoretical relationship in Equation 18. Gray dashed line denotes $D = D_0$. (b–e) Zoom-in views of simulations with $f_0 = $ (b) 0.39, (c) 0.44, (d) 0.52, and (e) the most critical cases. Green dashed curves are the relationship between the squared amplification factor λ^2 and the fault stress parameter T for $\lambda \ll 1$ and $\lambda \gg 1$ from Figure 2 in Sáez et al. (2022).

6. Seismicity Back-Front

In addition to the seismicity front, our simulations that include stress interactions produce a back-front: a later front behind which seismicity is largely absent (Figure 10). While this region rarely experiences earthquake nucleation, rupture from larger events may still propagate into it. Like the seismicity front, the back-front also exhibits a diffusive migration pattern, with a lower apparent diffusivity.

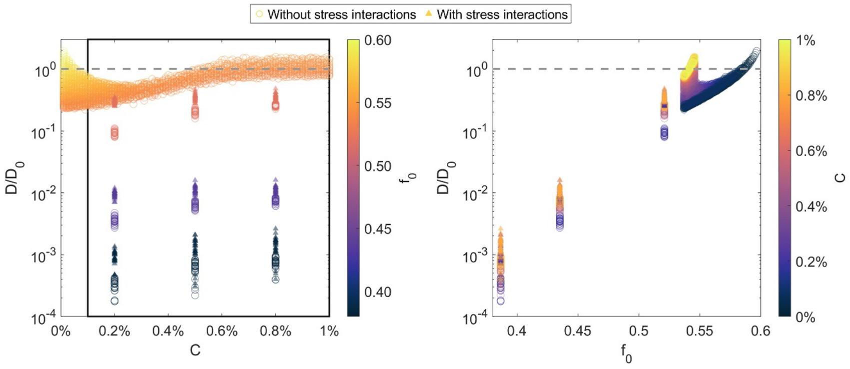

Figure 15. D/D_0 as a function of C (left) and f_0 (right) from simulations with stress interactions (filled symbols) and without stress interactions (empty symbols). Gray dashed line denotes $D = D_0$. Black rectangle denotes the realistic range of C.

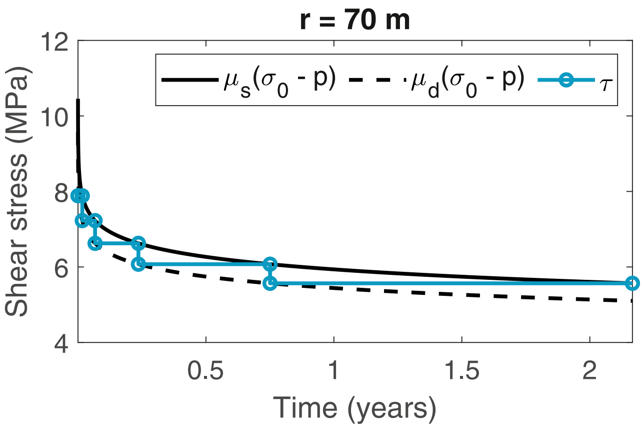

Figure 16. Example of stress and strength changes at a distance of 70 m.

In Section 6.1, we reveal that the seismicity rate decreases over time without accounting for stress interactions, indicating a natural suppression of activity near the injector ongoing injection. In Section 6.2, we demonstrate that stress interactions are essential to generate a distinct and diffusive back-front, suppressing seismicity in the vicinity of the injector.

6.1. Near-Well Seismicity Rate Decrease

A decrease in the seismicity rate is a natural consequence of constant injection over a long period of time. To illustrate this, we present a simplified analytical derivation in a model that excludes stress interactions, focusing solely on the strength changes due to changes in pore pressure and stress drop inside rupture areas. Under this assumption, we consider a fault patch with initial normal stress σ_0, and examine its stress evolution in response to fluid injection.

Following a rupture event, the shear stress of the ruptured fault patch is reduced due to frictional weakening to:

$$\tau = \mu_d(\sigma_0 - p(t)) \tag{26}$$

where $p(t)$ is the pore pressure change at the time of rupture. This shear stress value remains constant until the next rupture event occurs, at the time $t + dt$ when the patch reaches the failure condition again, as shown in Figure 16:

$$\tau = \mu_s(\sigma_0 - p(t + dt)) \tag{27}$$

Therefore

$$\mu_s(\sigma_0 - p(t + dt)) = \mu_d(\sigma_0 - p(t)) \tag{28}$$

Approximating the pore pressure evolution by a first-order Taylor expansion,

$$p(t + dt) = p(t) + p'(t)dt \tag{29}$$

we rewrite Equation 28 as

$$\mu_s p'(t)dt = (\sigma_0 - p(t))(\mu_s - \mu_d) \tag{30}$$

The local seismicity rate $R(t)$ of this patch is inversely proportional to the earthquake recurrence interval dt, thus

$$R(t) = \frac{1}{dt} = \frac{\mu_s}{\mu_s - \mu_d}\frac{p'(t)}{\sigma_0 - p(t)} \tag{31}$$

In our injection scenario at constant flow rate, $p'(r,t) = \frac{\dot{m}_b \eta}{4\pi\rho_w kht} e^{-\frac{r^2}{4D_0 t}}$. As pore pressure diffuses, we expect the p' term in Equation 31 to dominate the temporal evolution of seismicity, causing the seismicity rate to decrease over time. We illustrate this by an example: Figure 17a shows the evolution of seismicity rate after the first rupture time, assuming the same initial stress as in Figure 2b. To validate Equation 31, we compute the spatio-temporal density of seismicity from the simulation shown in Figure 8b. The resulting seismicity density (Figure 17b) is in good agreement with the prediction by Equation 31 (Figure 17a). This example illustrates how continuous injection with a constant flow flux leads to a gradual decline in seismicity. However, this seismicity rate reduction does not have a spatio-temporal pattern characteristic of a back-front.

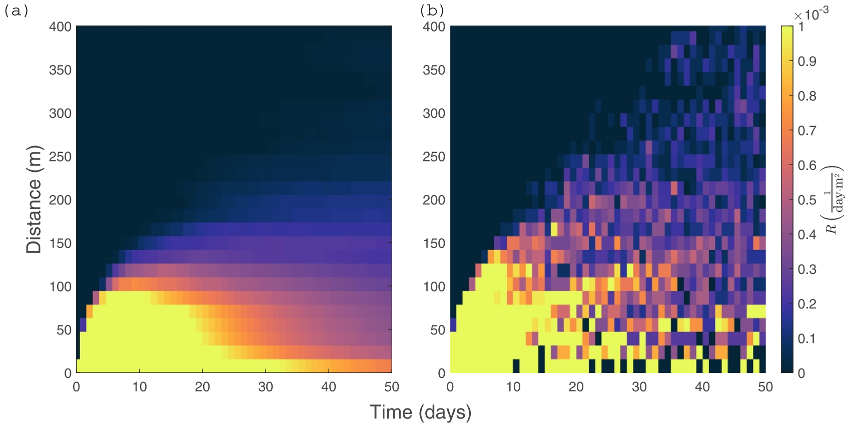

Figure 17. Seismicity rate of (a) estimation from Equation 31 and (b) numerical simulation (using a time window of 5 days and a distance interval of 16 m).

6.2. Stress Interactions Control Back-Front

While Section 6.1 shows that pressure-driven rupture events without stress interactions can lead to a gradual decrease in seismicity rate over time, it does not produce a sharp propagating back-front. In contrast, when stress interactions are included, our simulations reveal a migrating back-front with a diffusive pattern as shown in Figure 10. This suggests that stress interactions are essential for generating the back-front migration pattern.

To quantitatively characterize the back-front, we adopt a selection procedure similar to that used for the seismicity front. Rupture events are selected if their distances to the injector fall between the 5th and 20th percentiles within a 5-day sliding window. From Figure 18, we notice that the origin of back-front might be attributed to the stress redistribution caused by larger rupture events near the injection. Rupture events are triggered earlier in the vicinity of the injector, transferring stress to the surrounding area and progressively bringing neighboring patches closer to failure. As injection continues, larger rupture events occur, breaking a broader area and producing greater Coulomb stress changes. This leaves these fault patches farther from reactivation, and develops a back-front as fluid diffuses outward from the injector.

To examine the factors controlling back-front behavior, we analyze the apparent diffusivity of back-fronts from the same ensemble of simulations generated with 30 different random seeds for each roughness amplitude and stress environment (Figure 19). Our results show that back-front migration is generally faster in higher stress environments. This can be explained by a greater proportion of critical patches, which promotes more extensive rupture during early injection stages. When comparing different roughness amplitudes, the results reveal that back-fronts tend to propagate slightly faster on smoother faults. This is likely because stress transfers more effectively along smoother faults, which allows for earlier and larger rupture areas and further inhibits subsequent ruptures near the injector.

We also notice the importance of spatial arrangements of critical patches when we compare the simulations with the same roughness amplitude but different random seeds. Models with more critical fault patches near the injector have the potential to break larger areas. These events induce substantial static stress drops, which move the surrounding region farther from criticality and inhibit subsequent rupture. As a result, seismicity progressively shifts away from the injection point, producing a clear back-front. Figure 20 presents two simulations with the same roughness amplitude and background stress conditions but different random seeds, leading to different spatial arrangements of critical patches. The simulations demonstrate significantly different back-front evolution, highlighting how the criticality of the area near the injector controls back-front migration.

While the emergence of a back-front has typically been associated with the post-injection period (Parotidis et al., 2004; Sáez & Lecampion, 2023), recent observations show that back-fronts can also occur during injection (De Barros et al., 2019; Ross & Cochran, 2021). De Barros et al. (2024) interpret this as an increase in earthquake nucleation length at high pore pressure, which makes fault patches aseismic. In Kim et al. (2025), seismicity near the injection well decays naturally due to the exhaustion of available nucleation sources over a short timescale. In

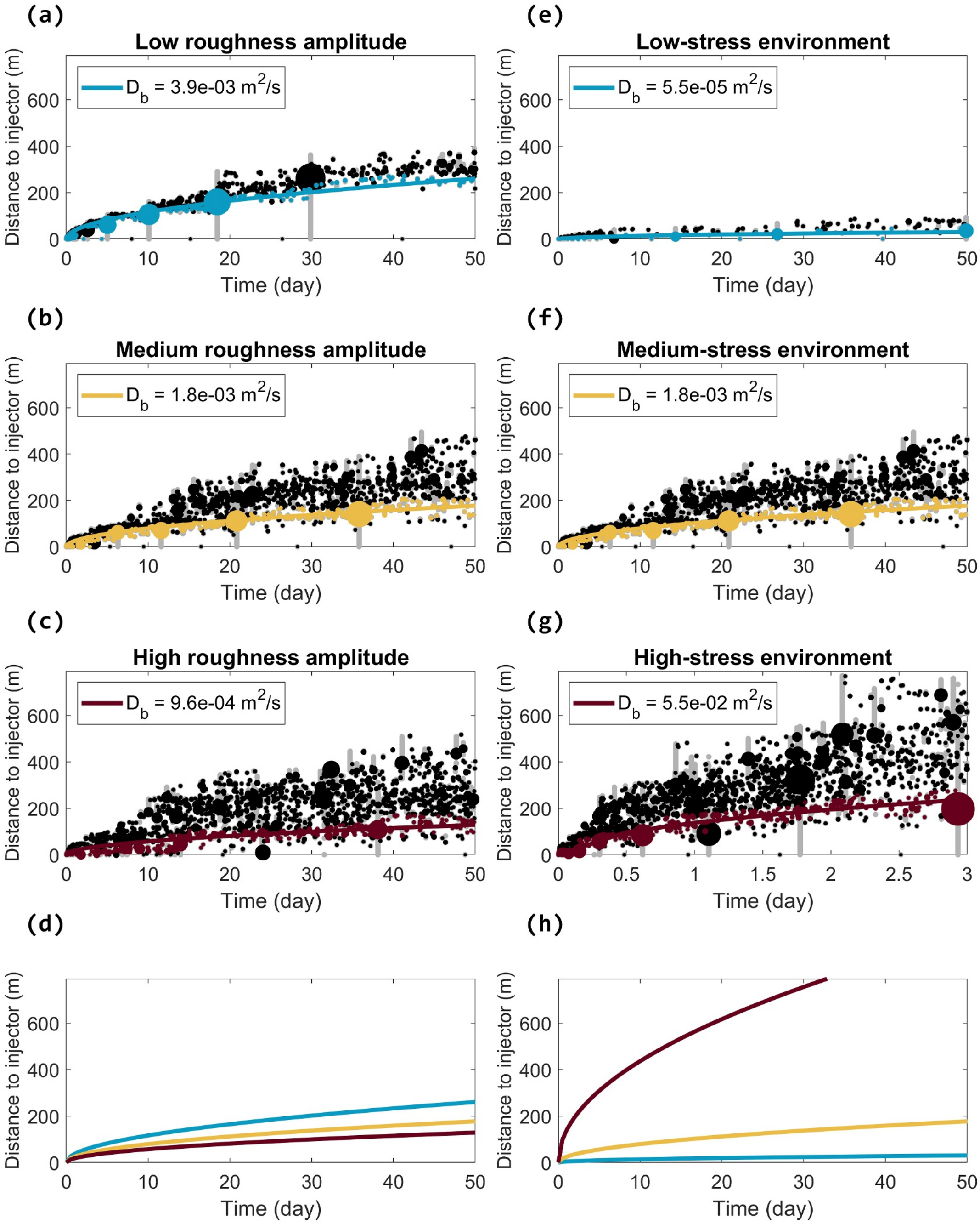

Figure 18. Spatio-temporal evolution of seismicity at (a) low (b, e–g) medium and (c) high roughness amplitudes in (e) low (f, a–c) medium and (g) high stress environments with stress interactions. Black circles indicate the location (distance to injector) and occurrence time of earthquakes. Colored circles and curves correspond to the back-front and the best-fitting to a square root function. (d) Comparison of the fitted seismicity front with the corresponding colors in (a–c) for different roughness amplitudes. (h) Comparison of the fitted back-front with the corresponding colors in (e–g) for different initial stress environments.

our model, the back-front is driven by early stage relatively large rupture events close to the injector. These differences imply diagnostic observational signatures. A reduced rate of small events would be characteristic of the conditional stability mechanism of De Barros et al. (2024), whereas the presence of early stage relatively large rupture events could favor our proposed mechanism. In reality these three mechanisms could co-exist.

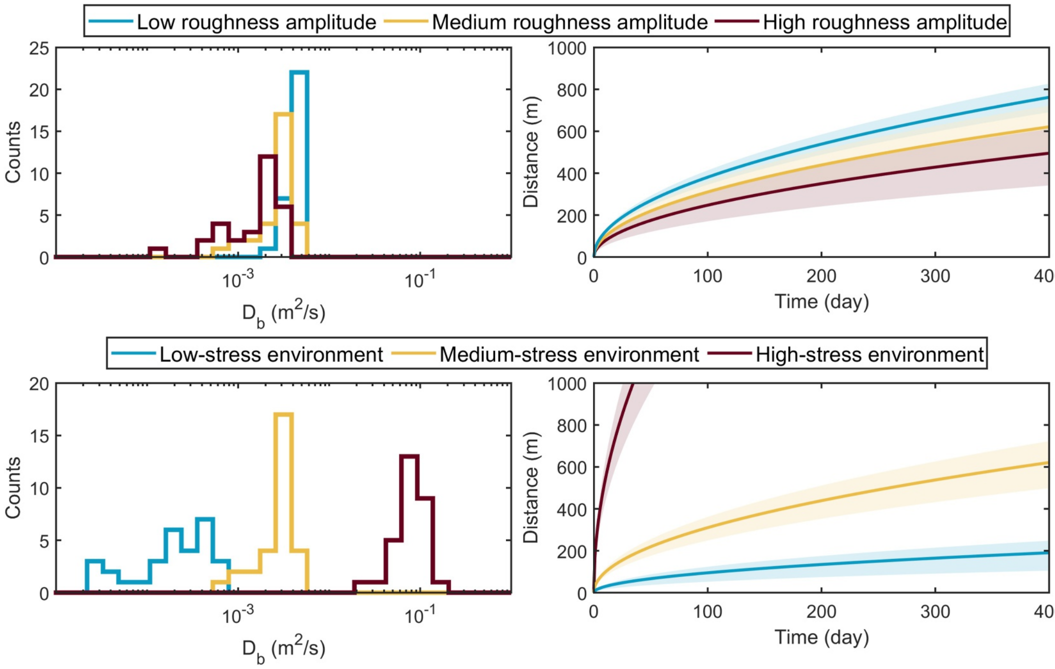

Figure 19. (left) Histograms of the apparent diffusivity of the back-front for sets of 90 simulations with stress interactions at 3 roughness amplitudes (top) and 3 initial stress environments (bottom). (right) Comparison of the fitted back-front associated with the mean values of apparent diffusivity for different roughness amplitudes (top) and initial stress environments (bottom). The shaded areas represent the standard deviation of apparent diffusivity for each case.

7. Discussion: Rationale of Our Reference Model and Its Limitations

Our primary objective is to focus on the effect of fault roughness on seismicity migration, deliberately excluding any additional potential heterogeneities or complexities. The proposed model should be considered a reference model that isolates the influence of fault roughness on seismicity migration. In the future, this reference model could serve as a foundation for understanding the outcomes of more advanced models that incorporate additional factors that may compete against or enhance the effect of fault roughness. While other sources of heterogeneity (e.g., lithological variations or frictional properties) may also influence seismicity migration, the goal is to avoid adding stochastic heterogeneities that are poorly constrained to the model and to focus on fault roughness, for which physical constraints on spatial distribution are available.

This simple reference model builds upon previous studies (e.g., Bhattacharya & Viesca, 2019; Hummel & Shapiro, 2012; Rothert & Shapiro, 2007; Sáez et al., 2022; Shapiro et al., 1997; Talwani & Acree, 1984) where

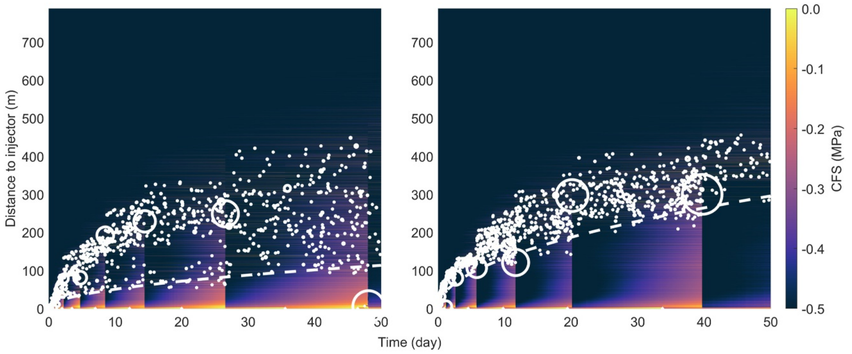

Figure 20. Slower (left) and faster (right) back-fronts in two simulations with the same $C = 0.5\%$ and $f_0 = 0.44$ but different random seeds. White circles denote the hypocenters of the rupture events. Background color shows the spatio-temporal evolution of Coulomb stress. White dashed curve is the best-fitting to a square root function for back-front.

many of the modeling assumptions are similar. Regarding fluid pressure diffusion, these studies also considered analytical solutions that ignore geological complexities such as permeability contrasts between the main slip surface and damage zone. The potential coupling between earthquake slips and permeability changes (e.g., Berrios-Rivera et al., 2025; Elsworth et al., 2025; Yu et al., 2024) is also excluded. Similarly, the coupling between roughness and fluid flow (e.g., Acosta et al., 2020) is not included. Both earthquake slip and fault roughness can influence the non-linear diffusion of pore pressure, potentially affecting the migration speed of seismicity (Haagenson & Rajaram, 2021).

Regarding initial stresses, the reference model assumes a depth-dependent background stress state, resulting in spatially variable normal and shear stresses due to fault roughness. However, slip events from tectonic earthquakes occurring prior to fluid injection can also induce pre-stress changes (Dempsey & Suckale, 2016; Marsan, 2006), which are not considered in this model. Both pre-stress heterogeneities caused by fault roughness, as considered here, and those caused by tectonic slip events, can potentially affect the migration pattern of induced seismicity.

Regarding fault friction, a simple friction law is employed. The use of more complex friction laws (e.g., Bhattacharya & Viesca, 2019; De Barros et al., 2024; Kim & Avouac, 2023; Kim et al., 2025; Sáez et al., 2022) showed that the earthquake nucleation process governed by the rate-and-state friction law can slow down the seismicity front.

Regarding induced stresses, the model is kept simple, as in previous studies (e.g., Bhattacharya & Viesca, 2019; Hummel & Shapiro, 2012; Rothert & Shapiro, 2007; Sáez et al., 2022; Shapiro et al., 1997; Talwani & Acree, 1984), considering only changes in effective normal stress due to an increase in fluid pressure. Potential poroelastic and thermoelastic stress changes resulting from the injection of cold fluid through a fracture or fault are not modeled. In the case of injection through a single fracture, poroelastic stress changes are expected to be minimal. However, cooling of the fault could lead to significant localized stress changes near the injector (Marelis et al., 2024; Mossop, 2001), which might influence seismicity migration.

8. Conclusions

We develop a simple physics-based model to investigate the influence of fault roughness and stress interactions on the spatio-temporal evolution of injection-induced seismicity. To isolate the effect of fault roughness, we consider heterogeneity in our model to arise solely from fault roughness.

We demonstrate that the apparent diffusivity of seismicity fronts, which is often inferred from seismicity migration patterns, can differ significantly from the hydraulic diffusivity. Our model indicates that, on realistically rough faults, seismicity generally migrates more slowly than the nominal pressure front. In particular, faults in relatively low initial stress environments, especially those with low roughness amplitudes, tend to exhibit slow seismicity migration, resulting in an apparent diffusivity far below the hydraulic diffusivity. In rare cases, when faults are very close to criticality ($P_c \leq 0.2P_v$) and relatively rough ($C > 0.5\%$), the apparent diffusivity can exceed the hydraulic diffusivity, indicating that the seismicity front can outpace the nominal pressure front.

In addition to the seismicity front, our simulations reveal the presence of back-fronts, which marks regions where seismicity is inhibited. While often attributed to shut-in effects, our results show that back-fronts can develop during continuous injection. These patterns result from early stage stress redistribution following stress drops close to the injector, which move nearby fault patches farther from criticality.

Our results highlight that taking fault roughness into account is essential to better reflect realistic stress distribution and assess seismicity migration behavior. Our findings emphasize the importance of considering both fault roughness and initial stress environment when interpreting seismicity migration in terms of fluid pressure diffusion. Misinterpreting apparent diffusivity as hydraulic diffusivity can lead to significant errors in estimating subsurface properties, especially when the initial stress environment is far from criticality. Increasing fault roughness produces a larger proportion of critically stressed fault patches and thus accelerates the seismicity migration. Hence, fault roughness and initial stress environment together control the seismicity migration speed through their impact on the spatial distribution of critical pressure P_c.

Conflict of Interest

The authors declare no conflicts of interest relevant to this study.

Data Availability Statement

The first version of the numerical modeling performed in this study will be archived at Lin et al. (2025).

Acknowledgments
Emily Brodsky shared codes for rough surface generation. Reviews by Eric Dunham, So Ozawa, and an anonymous reviewer, together with suggestions from the Editor Douglas Schmitt on a previous draft, helped improve this manuscript. HFL was funded by an EUR Spectrum graduate fellowship of Université Côte d'Azur and by TNO. This work was supported by the French government through the UCAJEDI Investments in the Future project (ANR-15-IDEX-01) managed by the National Research Agency (ANR). Open access publication funding provided by COUPERIN CY26.

References

Abramowitz, M., & Stegun, I. A. (1948). *Handbook of mathematical functions with formulas, graphs, and mathematical tables* (Vol. 55). US Government printing office.

Acosta, M., Maye, R., & Violay, M. (2020). Hydraulic transport through calcite bearing faults with customized roughness: Effects of normal and shear loading. *Journal of Geophysical Research: Solid Earth*, *125*(8), e2020JB019767. https://doi.org/10.1029/2020JB019767

Bear, J. (1979). *Hydraulics of groundwater*. Dover Publications Inc.

Berrios-Rivera, N., Ozawa, S., & Dunham, E. M. (2025). Fluid pressure diffusion and elastic stress transfer from seismic slip control slip front expansion in fluid-driven swarm seismicity. *Journal of Geophysical Research: Solid Earth*, *130*(12), e2025JB032438. https://doi.org/10.1029/2025JB032438

Bhattacharya, P., & Viesca, R. C. (2019). Fluid-induced aseismic fault slip outpaces pore-fluid migration. *Science*, *364*(6439), 464–468. https://doi.org/10.1126/SCIENCE.AAW7354

Brodsky, E. E., Kirkpatrick, J. D., & Candela, T. (2016). Constraints from fault roughness on the scale-dependent strength of rocks. *Geology*, *44*(1), 19–22. https://doi.org/10.1130/G37206.1

Brown, S. R. (1987). Fluid flow through rock joints: The effect of surface roughness. *Journal of Geophysical Research*, *92*(B2), 1337–1347. https://doi.org/10.1029/JB092iB02p01337

Candela, T., Ampuero, J. P., Diederik, J., Wees, V., Fokker, P., & Wassing, B. (2019). Semi-analytical fault injection model: Effect of fault roughness and injection scheme on induced seismicity. In *European Geothermal Conference* (pp. 11–14). European Geothermal Congress 2019 Den Haag.

Candela, T., Renard, F., Bouchon, M., Brouste, A., Marsan, D., Schmittbuhl, J., & Voisin, C. (2009). Characterization of fault roughness at various scales: Implications of three-dimensional high resolution topography measurements. *Pure and Applied Geophysics*, *166*(10–11), 1817–1851. https://doi.org/10.1007/S00024-009-0521-2

Candela, T., Renard, F., Klinger, Y., Mair, K., Schmittbuhl, J., & Brodsky, E. E. (2012). Roughness of fault surfaces over nine decades of length scales. *Journal of Geophysical Research*, *117*(B8). https://doi.org/10.1029/2011JB009041

Cappa, F., Guglielmi, Y., Nussbaum, C., De Barros, L., & Birkholzer, J. (2022). Fluid migration in low-permeability faults driven by decoupling of fault slip and opening. *Nature Geoscience*, *15*(9), 747–751. https://doi.org/10.1038/s41561-022-00993-4

Cappa, F., & Rutqvist, J. (2011). Impact of CO_2 geological sequestration on the nucleation of earthquakes. *Geophysical Research Letters*, *38*(17). https://doi.org/10.1029/2011GL048487

Dake, L. (1978). *Fundamentals of reservoir engineering*. Elsevier.

Danré, P., Garagash, D., Barros, L. D., Cappa, F., & Ampuero, J.-P. (2024). Control of seismicity migration in earthquake swarms by injected fluid volume and aseismic crack propagation. *Journal of Geophysical Research: Solid Earth*, *129*(1), e2023JB027276. https://doi.org/10.1029/2023JB027276

De Barros, L., Baques, M., Godano, M., Helmstetter, A., Deschamps, A., Larroque, C., & Courboulex, F. (2019). Fluid-induced swarms and Coseismic stress transfer: A dual process highlighted in the aftershock sequence of the 7 April 2014 earthquake (Ml 4.8, Ubaye, France). *Journal of Geophysical Research: Solid Earth*, *124*(4), 3918–3932. https://doi.org/10.1029/2018JB017226

De Barros, L., Danré, P., Garagash, D., Cappa, F., & Lengliné, O. (2024). Systematic observation of a seismic back-front during fluid injection in both natural and anthropogenic earthquake swarms. *Earth and Planetary Science Letters*, *641*, 118849. https://doi.org/10.1016/J.EPSL.2024.118849

De Barros, L., Wynants-Morel, N., Cappa, F., & Danré, P. (2021). Migration of fluid-induced seismicity reveals the seismogenic State of faults. *Journal of Geophysical Research: Solid Earth*, *126*(11), e2021JB022767. https://doi.org/10.1029/2021JB022767

Deichmann, N., & Giardini, D. (2009). Earthquakes induced by the stimulation of an enhanced geothermal system below Basel (Switzerland). *Seismological Research Letters*, *80*(5), 784–798. https://doi.org/10.1785/gssrl.80.5.784

Dempsey, D., & Suckale, J. (2016). Collective properties of injection-induced earthquake sequences: 1. Model description and directivity bias. *Journal of Geophysical Research: Solid Earth*, *121*(5), 3609–3637. https://doi.org/10.1002/2015JB012550

Dieterich, J. H., & Smith, D. E. (2009). Nonplanar faults: Mechanics of slip and off-fault damage. *Pure and Applied Geophysics*, *166*(10–11), 1799–1815. https://doi.org/10.1007/s00024-009-0517-y

Doan, M. L., Brodsky, E. E., Kano, Y., & Ma, K. F. (2006). In situ measurement of the hydraulic diffusivity of the active Chelungpu fault, Taiwan. *Geophysical Research Letters*, *33*(16). https://doi.org/10.1029/2006GL026889

Ellsworth, W. L. (2013). Injection-induced earthquakes. *Science*, *341*(6142), 1225942. https://doi.org/10.1126/SCIENCE.1225942

Elsworth, D., Li, Z., Yu, P., An, M., Zhang, F., Huang, R., et al. (2025). Constraints on triggered seismicity and its control on permeability evolution. *Journal of Rock Mechanics and Geotechnical Engineering*, *17*(1), 20–30. https://doi.org/10.1016/J.JRMGE.2024.11.035

Eyre, T. S., Zecevic, M., Salvage, R. O., & Eaton, D. W. (2020). A long-lived swarm of hydraulic fracturing-induced seismicity provides evidence for Aseismic slip. *Bulletin of the Seismological Society of America*, *110*(5), 2205–2215. https://doi.org/10.1785/0120200107

Fang, Z., & Dunham, E. M. (2013). Additional shear resistance from fault roughness and stress levels on geometrically complex faults. *Journal of Geophysical Research: Solid Earth*, *118*(7), 3642–3654. https://doi.org/10.1002/jgrb.50262

Faraudo, J. (2002). Diffusion equation on curved surfaces. I. Theory and application to biological membranes. *The Journal of Chemical Physics*, *116*(13), 5831–5841. https://doi.org/10.1063/1.1456024

Garagash, D. I., & Germanovich, L. N. (2012). Nucleation and arrest of dynamic slip on a pressurized fault. *Journal of Geophysical Research*, *117*(B10). https://doi.org/10.1029/2012JB009209

Guglielmi, Y., Elsworth, D., Cappa, F., Henry, P., Gout, C., Dick, P., & Durand, J. (2015). In situ observations on the coupling between hydraulic diffusivity and displacements during fault reactivation in shales. *Journal of Geophysical Research: Solid Earth*, *120*(11), 7729–7748. https://doi.org/10.1002/2015JB012158

Haagenson, R., & Rajaram, H. (2021). Seismic diffusivity and the influence of heterogeneity on injection-induced seismicity. *Journal of Geophysical Research: Solid Earth*, *126*(6), e2021JB021768. https://doi.org/10.1029/2021JB021768

Hummel, N., & Shapiro, S. A. (2012). Microseismic estimates of hydraulic diffusivity in case of non-linear fluid-rock interaction. *Geophysical Journal International*, *188*(3), 1441–1453. https://doi.org/10.1111/J.1365-246X.2011.05346.X

Jaeger, J. C., Cook, N. G. W., & Zimmerman, R. (2009). *Fundamentals of rock mechanics*. Blackwell.

Kim, T., & Avouac, J.-P. (2023). Stress-based and convolutional forecasting of injection-induced seismicity: Application to the Otaniemi geothermal reservoir stimulation. *Journal of Geophysical Research: Solid Earth*, *128*(4), e2022JB024960. https://doi.org/10.1029/2022JB024960

Kim, T., Im, K., & Avouac, J.-P. (2025). Finite size effects on seismicity induced by fluid injection in a discrete fault network with rate-and-State friction. *Journal of Geophysical Research: Solid Earth*, *130*(7), e2024JB030243. https://doi.org/10.1029/2024JB030243

Lin, H.-F., Ampuero, J. P., & Candela, T. (2025). Source code for fault roughness controls seismicity front migration during fluid injection [Software]. *Zenodo*. https://doi.org/10.5281/zenodo.17648844

Marelis, A., Beekman, F., & van Wees, J.-D. (2024). 3D mechanical analysis of geothermal reservoir operations in faulted sedimentary aquifers using MACRIS. *Geothermal Energy*, *12*(1), 5. https://doi.org/10.1186/s40517-024-00284-8

Marsan, D. (2006). Can Coseismic stress variability suppress seismicity shadows? Insights from a rate-and-state friction model. *Journal of Geophysical Research*, *111*(6). https://doi.org/10.1029/2005JB004060

Martínez-Garzón, P., Kwiatek, G., Sone, H., Bohnhoff, M., Dresen, G., & Hartline, C. (2014). Spatiotemporal changes, faulting regimes, and source parameters of induced seismicity: A case study from the geysers geothermal field. *Journal of Geophysical Research: Solid Earth*, *119*(11), 8378–8396. https://doi.org/10.1002/2014JB011385

Maurer, J. (2024). Statistical distribution of static stress resolved onto geometrically-rough faults. *Seismica*, *3*(2), 1–12. https://doi.org/10.26443/SEISMICA.V3I2.1206

Mossop, A. P. (2001). *Seismicity, subsidence and strain at the geysers geothermal field* (Unpublished Doctoral Dissertation). Stanford University.

Nikkhoo, M., & Walter, T. R. (2015). Triangular dislocation: An analytical, artefact-free solution. *Geophysical Journal International*, *201*(2), 1119–1141. https://doi.org/10.1093/GJI/GGV035

Ozawa, S. W., Hatano, T., & Kame, N. (2019). Longer migration and spontaneous decay of aseismic slip pulse caused by fault roughness. *Geophysical Research Letters*, *46*(2), 636–643. https://doi.org/10.1029/2018GL081465

Parotidis, M., Shapiro, S. A., & Rothert, E. (2004). Back front of seismicity induced after termination of borehole fluid injection. *Geophysical Research Letters*, *31*(2). https://doi.org/10.1029/2003GL018987

Power, W. L., & Tullis, T. E. (1991). Euclidean and fractal models for the description of rock surface roughness. *Journal of Geophysical Research*, *96*(B1), 415–424. https://doi.org/10.1029/90JB02107

Power, W. L., Tullis, T. E., Brown, S. R., Boitnott, G. N., & Scholz, C. H. (1987). Roughness of natural fault surfaces. *Geophysical Research Letters*, *14*(1), 29–32. https://doi.org/10.1029/GL014i001p00029

Ross, Z. E., & Cochran, E. S. (2021). Evidence for latent crustal fluid injection transients in Southern California from long-duration earthquake swarms. *Geophysical Research Letters*, *48*(12), e2021GL092465. https://doi.org/10.1029/2021GL092465

Rothert, E., & Shapiro, S. A. (2007). Statistics of fracture strength and fluid-induced microseismicity. *Journal of Geophysical Research*, *112*(B4). https://doi.org/10.1029/2005JB003959

Rutqvist, J., Wu, Y. S., Tsang, C. F., & Bodvarsson, G. (2002). A modeling approach for analysis of coupled multiphase fluid flow, heat transfer, and deformation in fractured porous rock. *International Journal of Rock Mechanics and Mining Sciences*, *39*(4), 429–442. https://doi.org/10.1016/S1365-1609(02)00022-9

Sáez, A., & Lecampion, B. (2023). Post-injection aseismic slip as a mechanism for the delayed triggering of seismicity. *Proceedings of the Royal Society A: Mathematical, Physical and Engineering Sciences*, *479*, 20220810. https://doi.org/10.1098/rspa.2022.0810

Sáez, A., & Lecampion, B. (2024). Fluid-driven slow slip and earthquake nucleation on a slip-weakening circular fault. *Journal of the Mechanics and Physics of Solids*, *183*, 105506. https://doi.org/10.1016/j.jmps.2023.105506

Sáez, A., Lecampion, B., Bhattacharya, P., & Viesca, R. C. (2022). Three-dimensional fluid-driven stable frictional ruptures. *Journal of the Mechanics and Physics of Solids*, *160*, 104754. https://doi.org/10.1016/j.jmps.2021.104754

Segall, P., & Lu, S. (2015). Injection-induced seismicity: Poroelastic and earthquake nucleation effects. *Journal of Geophysical Research: Solid Earth*, *120*(7), 5082–5103. https://doi.org/10.1002/2015JB012060

Shapiro, S. A., Huenges, E., & Borm, G. (1997). Estimating the crust permeability from fluid-injection-induced seismic emission at the KTB site. *Geophysical Journal International*, *131*(2), 15–23. https://doi.org/10.1111/j.1365-246X.1997.tb01215.x

Shapiro, S. A., Rothert, E., Rath, V., & Rindschwentner, J. (2002). Characterization of fluid transport properties of reservoirs using induced microseismicity. *Geophysics*, *67*(1), 212–220. https://doi.org/10.1190/1.1451597

Tal, Y., Hager, B. H., & Ampuero, J. P. (2018). The effects of fault roughness on the earthquake nucleation process. *Journal of Geophysical Research: Solid Earth*, *123*(1), 437–456. https://doi.org/10.1002/2017JB014746

Talwani, P., & Acree, S. (1984). Pore pressure diffusion and the mechanism of reservoir-induced seismicity. *Pure and Applied Geophysics*, *122*(6), 947–965. https://doi.org/10.1007/BF00876395

Theis, C. V. (1935). The relation between the lowering of the Piezometric surface and the rate and duration of discharge of a well using groundwater storage. *Eos, Transactions American Geophysical Union*, *16*(2), 519–524. https://doi.org/10.1111/jawr.1965.1.3.9

Wang, L., Kwiatek, G., Renard, F., Guérin-Marthe, S., Rybacki, E., Bohnhoff, M., et al. (2024). Fault roughness controls injection-induced seismicity. *Proceedings of the National Academy of Sciences*, *121*(3), e2310039121. https://doi.org/10.1073/PNAS.2310039121

Witherspoon, P. A., Wang, J. S. Y., Iwai, K., & Gale, J. E. (1979). Validity of Cubic Law for fluid flow in a deformable rock fracture. *Water Resources Research*, *16*(6), 1016–1024. https://doi.org/10.1029/WR016i006p01016

Wynants-Morel, N., Cappa, F., De Barros, L., & Ampuero, J. P. (2020). Stress perturbation from aseismic slip drives the seismic front during fluid injection in a permeable fault. *Journal of Geophysical Research: Solid Earth*, *125*(7), e2019JB019179. https://doi.org/10.1029/2019JB019179

Yu, P., Mali, A., Velaga, T., Bi, A., Yu, J., Marone, C., et al. (2024). Crustal permeability generated through microearthquakes is constrained by seismic moment. *Nature Communications*, *15*(1), 2057. https://doi.org/10.1038/s41467-024-46238-3

Zielke, O., Galis, M., & Mai, P. M. (2017). Fault roughness and strength heterogeneity control earthquake size and stress drop. *Geophysical Research Letters*, *44*(2), 777–783. https://doi.org/10.1002/2016GL071700